2015

Discovery of Large Molecular Gas Reservoirs in Post-Starburst Galaxies

K. Decker French

Yujin Yang

Ann Zabludoff

Desika Narayanan
Haverford College, dnarayan@haverford.edu

The Astrophysical Journal, 801:1 (21pp), 2015 March 1 doi:10.1088/0004-637X/801/1/1

DISCOVERY OF LARGE MOLECULAR GAS RESERVOIRS IN POST-STARBURST GALAXIES

K. Decker French[1], Yujin Yang[2,3], Ann Zabludoff[1], Desika Narayanan[1,4], Yancy Shirley[1], Fabian Walter[5], John-David Smith[6], and Christy A. Tremonti[7]
[1] Steward Observatory, University of Arizona, 933 North Cherry Avenue, Tucson, AZ 85721, USA
[2] Argelander Institut für Astronomie, Universität Bonn, Auf dem Hügel 71, D-53121 Bonn, Germany
[3] Korea Astronomy and Space Science Institute, 776 Daedeokdae-ro, Yuseong-gu, Daejeon 305-348, Korea
[4] Department of Physics and Astronomy, Haverford College, 370 Lancaster Avenue, Haverford, PA 19041, USA
[5] Max-Planck-Institut für Astronomie, Königstuhl 17, D-69117 Heidelberg, Germany
[6] Department of Physics and Astronomy, University of Toledo, Ritter Obs., MS #113, Toledo, OH 43606, USA
[7] Department of Astronomy, University of Wisconsin-Madison, Madison, WI 53706, USA
Received 2014 May 30; accepted 2014 December 30; published 2015 February 23

ABSTRACT

Post-starburst (or "E+A") galaxies are characterized by low Hα emission and strong Balmer absorption, suggesting a recent starburst, but little current star formation. Although many of these galaxies show evidence of recent mergers, the mechanism for ending the starburst is not yet understood. To study the fate of the molecular gas, we search for CO(1–0) and (2–1) emission with the IRAM 30 m and SMT 10 m telescopes in 32 nearby ($0.01 < z < 0.12$) post-starburst galaxies drawn from the Sloan Digital Sky Survey. We detect CO in 17 (53%). Using CO as a tracer for molecular hydrogen, and a Galactic conversion factor, we obtain molecular gas masses of $M(H_2) = 10^{8.6}$–$10^{9.8}\,M_\odot$ and molecular gas mass to stellar mass fractions of $\sim 10^{-2}$–$10^{-0.5}$, comparable to those of star-forming galaxies. The large amounts of molecular gas rule out complete gas consumption, expulsion, or starvation as the primary mechanism that ends the starburst in these galaxies. The upper limits on $M(H_2)$ for the 15 undetected galaxies range from $10^{7.7}\,M_\odot$ to $10^{9.7}\,M_\odot$, with the median more consistent with early-type galaxies than with star-forming galaxies. Upper limits on the post-starburst star formation rates (SFRs) are lower by $\sim 10\times$ than for star-forming galaxies with the same $M(H_2)$. We also compare the molecular gas surface densities (Σ_{H_2}) to upper limits on the SFR surface densities (Σ_{SFR}), finding a significant offset, with lower Σ_{SFR} for a given Σ_{H_2} than is typical for star-forming galaxies. This offset from the Kennicutt–Schmidt relation suggests that post-starburst galaxies have lower star formation efficiency, a low CO-to-H_2 conversion factor characteristic of ultraluminous infrared galaxies, and/or a bottom-heavy initial mass function, although uncertainties in the rate and distribution of current star formation remain.

Key words: galaxies: evolution – radio lines: galaxies

1. INTRODUCTION

Post-starburst (or "E+A") galaxies show signs of being caught in the middle of a dramatic, but brief, stage in their evolution. Emission line indicators suggest little-to-no current star formation, but strong Balmer absorption lines indicate a population of A stars that formed in a substantial burst of star formation before a sudden stop ~1 Gyr ago (Dressler & Gunn 1983; Couch & Sharples 1987).

Post-starburst galaxies are likely in transition between star-forming gas-rich disk galaxies and passively evolving gas-poor early types. Their disturbed morphologies indicate that many are post-merger, and most have spheroid-dominated kinematics (Zabludoff et al. 1996; Norton et al. 2001; Yang et al. 2004, 2008). Many have blue cores, which can fade into the color gradients observed in early type galaxies (Yamauchi & Goto 2005; Yang et al. 2006, 2008), and many lie in the "green valley" of the color–magnitude diagram (Wong et al. 2012). Although only ~0.2% of local galaxies are post-starbursts, the short duration of this phase suggests that ~40% of galaxies could have passed through it (Zabludoff et al. 1996; Snyder et al. 2011).

A critical part of galaxy evolution is the end, or possible "quenching," of star formation. As transitional objects, post-starburst galaxies serve as a unique laboratory for understanding the processes that drive this cessation. Explanations for the end of the starburst fall into two general categories: elimination of the molecular gas or suppression of star formation.

One possibility is that the starburst uses up the dense molecular clouds in forming stars (Kennicutt 1998; Gao & Solomon 2004). Molecular gas could also be removed from the galaxy in outflows (Narayanan et al. 2008). Evidence of LINER activity and large outflows are seen in post-starbursts (Yan et al. 2006; Yang et al. 2006; Tremonti et al. 2007), and active galactic nuclei (AGNs) are observed to eject molecular gas in outflows (Feruglio et al. 2010), although the driver of the outflows in post-starbursts may be due to star formation, not AGN activity (Sell et al. 2014). Some environmental effects, such as starvation (e.g., Larson et al. 1980; Boselli & Gavazzi 2006), are thought to eliminate molecular gas reservoirs in galaxies. The molecular gas mass is several orders of magnitude lower in early types than in late types (e.g., Young et al. 2011; Crocker et al. 2011). If post-starbursts are becoming early types, they must lose or repurpose most of their gas.

Feedback mechanisms could be responsible for suppressing star formation, resulting in the end of the starburst. Molecular gas heating and suppressed star formation efficiency (SFE) have been claimed in galaxies with AGN (Nesvadba et al. 2010), resulting in higher observed molecular gas surface densities than the Kennicutt–Schmidt (KS) relation (Kennicutt 1998) would predict for their star formation rate (SFR) densities. Observations of cold gas in early type galaxies with AGN and recent bursts of star formation reveal little molecular gas ($<10^9\,M_\odot$), which declines steeply with the age since the last period of star formation (Schawinski et al. 2009). In our sample, the timescales necessary for outflows to expel the molecular gas from the galaxy are less than the time elapsed since the starburst ended (about 0.3–1 Gyr), so if AGN feedback has significantly reduced the molecular gas reservoirs, we should observe the galaxies in their depleted state.

A lower SFE is suggested in gas-rich, fast-rotating early type galaxies by Davis et al. (2014), who observe lower SFR surface densities than the molecular gas surface densities would predict by a factor of ∼2.5. These authors favor dynamical methods of lowering SFE in this sample of galaxies, such as morphological quenching (Martig et al. 2009), where the gravitational stability of the gas prevents it from collapsing and forming stars. Although post-starburst galaxies are likely to evolve into early types, it is not clear that the gas-rich sample studied by Davis et al. (2014) are on the same evolutionary sequence as post-starbursts.

We aim to test these explanations for the starbursts' end by constraining the properties of molecular gas within post-starbursts. Reservoirs of H I have been observed in post-starburst galaxies (Chang et al. 2001; Buyle et al. 2006; Zwaan et al. 2013). In six of the eleven post-starbursts targeted in these samples, H I 21 cm emission is detected, with atomic gas to stellar mass fractions typically between those of early and late type galaxies. However, H I is not a good tracer of star formation fuel (Kennicutt et al. 2007), and we must look at molecular gas signatures to understand the starbursts' end.

Detailed CO maps have been measured for only a handful of local post-starburst galaxies (Kohno et al. 2002; Alatalo et al. 2014). Even then, the two galaxies studied, NGC 5195 and NGC 1266, are not universally agreed upon as post-starbursts due to their Hα emission. The molecular gas in these galaxies is centrally concentrated, reaching starburst-like gas surface densities. Their kinematics led these authors to suggest morphological quenching (Martig et al. 2009), where the gravitational stability of the gas prevents it from collapsing and forming stars. There is a need for a survey of the molecular gas content in a representative sample of post-starburst galaxies.

We set out here to determine how much molecular gas remains in a sample of 32 post-starburst galaxies drawn from the Sloan Digital Sky Survey (SDSS; York et al. 2000), and to determine whether the molecular gas densities are consistent with the small or negligible levels of current star formation. We observe the CO(1–0) and CO(2–1) lines with the IRAM 30 m telescope, and observe a subset of 13 galaxies in CO(2–1) with the SMT or HHT 10 m telescope. By assuming that the CO traces H_2, we test whether the cessation of star formation was due to a lack of molecular gas, or to the gas being consumed by the burst, expelled in outflows, or prevented from entering the galaxy (starvation of H I; Larson et al. 1980). By comparing to the molecular gas versus SFR surface density relation for other galaxies, we will be able to determine if the SFE in post-starbursts is reduced by either gas heating, morphological quenching, or some other mechanism.

We discuss our sample and observations in Section 2. Measurements of molecular gas masses and comparisons to the SFRs are presented in Section 3. We test these results and consider their implications for galaxy evolution in Section 4, presenting our conclusions in Section 5. When needed, we assume a cosmology of $\Omega_m = 0.3$, $\Omega_\Lambda = 0.7$, and $h = 0.7$.

2. OBSERVATIONS AND DATA ANALYSIS

2.1. Sample Selection

Our parent sample is drawn from the SDSS main galaxy spectroscopic sample (Strauss et al. 2002), which is selected to have a limiting magnitude of $r < 17.77$ mag. The initial sample was selected from the SDSS DR7 (Abazajian et al. 2009), using the line fluxes and indices from the MPA-JHU catalogs (Aihara et al. 2011). We exclude galaxies with $z < 0.01$ to eliminate those that are very large on the sky relative to the 3″ diameter of the SDSS fibers. We also exclude galaxies with unreliable[7] Hα equivalent widths (EW), or median signal-to-noise (S/N) values of less than 10 pixel^{-1}. These cuts ensure that the line index measurements are reliable. Our final parent sample from DR10 is composed of 595,268 galaxies.

We select post-starburst galaxies from our parent sample by identifying galaxies with strong stellar Balmer absorption lines signifying a recent ($\lesssim$ Gyr) starburst but little nebular emission indicative of on-going star formation. We use the Lick Hδ index to characterize the stellar Balmer absorption. We require $H\delta_A - \sigma(H\delta_A) > 4$ Å, where $\sigma(H\delta_A)$ is the measurement error of the $H\delta_A$ index. We ensure that the galaxies have little on-going star formation by requiring Hα EW < 3 Å in the rest frame. These selection criteria result in a sub-sample of 1207 galaxies from the parent sample (0.20%).

We have chosen two sub-samples for *Hubble Space Telescope*, *Spitzer*, and *Herschel* imaging, which we follow-up here. Fifteen galaxies designated "S" throughout were selected to represent a variety of ages since the end of the burst and based on their projected 8 μm flux from SDSS spectra and serendipitous *Spitzer* observations. Galaxies with nearby companions and large [O III] EWs indicative of AGN activity were excluded. The post-burst ages are determined by fitting stellar population synthesis (SPS) models to the galaxy spectrum, assuming a combination of a young and old single burst stellar populations (K. D. French et al., in preparation). Seventeen galaxies designated "H" throughout were selected from their bright *Wide-field Infrared Survey Explorer* (*WISE*) 12 μm fluxes and again for a range of post-burst ages (although without the [O III] EW cut). More details on the "H" and "S" selection processes are available in A. Smercina et al. (in preparation). The effect of these selection criteria on properties of the resultant sample is studied in Section 4.1. Basic parameters of this sample are listed in Table 1.

2.2. IRAM 30 m CO Observations

Observations were carried out with the IRAM 30 m telescope over two observing campaigns in 2012 January (project ID: 218-11) and in 2012 August–September (ID: 074-12). We use the Eight Mixer Receiver (EMIR) to observe both CO(1–0) and CO(2–1) lines (rest frequency: 115.271 and 230.538 GHz). For each target, we tuned the 3 mm band (E090) and 1.3 mm band (E230) receivers to the redshifted CO(1–0) and CO(2–1) frequencies, $\nu_{obs} = 103.5$–113.5 GHz and 207.1–227.1 GHz, respectively. EMIR provides a bandwidth of 4 GHz in dual polarization corresponding to ∼11,000 and 5500 km s^{-1} for CO(1–0) and CO(2–1) lines, respectively. The Wideband Line Multiple Autocorrelator was used as the backend, with a resolution of 2 mHz corresponding to ∼5 km s^{-1} in the 3 mm band. Data were taken with a wobbler-switching mode with a frequency of 0.5 Hz or 1 Hz with a throw distance of 120″ in azimuth. The weather varied significantly: the precipitable water vapor ranged from 1 mm to 10 mm with medians of 3 mm (winter) and 6.8 mm (summer). Calibration was performed every 15 minutes with standard hot/cold load absorbers. The pointing was checked every 2 hr and was found to be stable within 3″. The FWHMs of beam are ≈22″ and 11″ for CO(1–0) and CO(2–1) lines, respectively.

We reduced the data with CLASS within the GILDAS software package[8] and IDL routines. We use the velocity intervals

[7] We require h_alpha_eqw_err > -1.

[8] http://www.iram.fr/IRAMFR/GILDAS

Table 1
Post-starburst Targets

Target	R.A. (deg)	Decl. (deg)	z	PlateID[a]	MJD[a]	FiberID[a]	$\log(M_*/M_\odot)$[b]	$D_n(4000)$ [c]	R_{90}[d] (arcsec)	$\mathrm{SFR_{lim}(H\alpha)}$[e] ($M_\odot$ yr^{-1})	$\mathrm{SFR_{lim}}(D_n(4000))$[f] ($M_\odot$ yr^{-1})	Ap. Corr.[g]
EAH01	128.640457	17.346207	0.0478	2276	53712	444	10.45	1.4122	9.35	0.0586	0.0149	6.5416
EAH02	141.580383	18.678055	0.0541	2360	53728	167	9.96	1.3798	5.26	0.0256	0.0271	3.5339
EAH03	222.066864	17.551651	0.0449	2777	54554	258	10.34	1.4227	7.06	0.0196	0.0055	6.3128
EAH04	318.502258	0.535107	0.0269	986	52443	468	10.18	1.2445	8.98	0.0674	0.0621	4.0061
EAH05	184.260117	39.077038	0.0653	2001	53493	473	10.00	1.4148	3.44	0.0625	0.0150	3.6750
EAH06	116.456268	31.378378	0.0441	755	52235	42	10.53	1.4477	5.52	0.3737	0.0221	2.8889
EAH07	167.824844	11.554388	0.0380	1604	53078	161	10.65	1.3226	12.50	0.2206	0.0292	9.8156
EAH08	147.077820	2.501155	0.0604	480	51989	580	10.41	1.3765	4.48	0.0407	0.0176	4.4127
EAH09	227.229538	37.558273	0.0291	1352	52819	610	10.21	1.3668	5.34	0.0572	0.0086	4.8709
EAH10	158.427979	21.127987	0.1053	2376	53770	454	10.24	1.4019	3.44	0.0419	0.0985	0.9470
EAH11	166.419617	5.998405	0.0542	1003	52641	87	10.61	1.4173	4.67	0.1690	0.0271	1.8951
EAH12	223.772690	13.281012	0.0826	2750	54242	18	10.55	1.4002	2.83	0.1834	0.0217	1.5728
EAH13	155.503281	22.163177	0.1129	2365	53739	624	11.00	1.2897	4.61	0.6212	0.5817	2.4663
EAH14	178.276855	64.299026	0.0622	598	52316	170	10.04	1.2878	3.15	0.1005	0.0272	2.1201
EAH15	163.085205	5.828218	0.0411	1001	52670	48	10.40	1.4178	4.72	0.0596	0.0258	5.6546
EAH16	141.740372	42.526840	0.1113	870	52325	208	10.74	1.1959	4.52	0.5076	5.2118	1.5974
EAH17	191.215393	−1.759901	0.0481	336	51999	469	10.05	1.4225	4.67	0.0479	0.0634	1.6746
EAS01	11.246839	−8.889684	0.0196	656	52148	404	10.24	1.4919	13.08	0.0130	0.0255	5.0585
EAS02	49.228809	−0.041979	0.0231	413	51929	238	10.08	1.4068	11.83	0.0253	0.0318	4.1478
EAS03	117.809624	34.418201	0.0628	756	52577	424	10.86	1.4849	7.46	0.1710	0.0083	6.8937
EAS04	126.755821	21.706779	0.0153	1927	53321	584	9.99	1.4244	8.84	0.0140	0.0091	45.2321
EAS05	146.112335	4.499120	0.0467	570	52266	537	10.57	1.3109	8.42	0.1078	0.0328	5.4079
EAS06	159.488983	46.244514	0.0227	962	52620	212	10.14	1.4450	7.10	0.0575	0.0055	1.3282
EAS07	169.781738	58.053974	0.0325	951	52398	128	10.54	1.4897	7.23	0.0447	0.1355	2.7343
EAS08	189.900208	12.438888	0.0408	1616	53169	71	10.67	1.3406	13.55	0.0550	0.1720	6.2527
EAS09	191.611816	50.792061	0.0270	1279	52736	362	10.56	1.5223	10.68	0.0432	0.0127	4.0306
EAS10	196.357605	53.591759	0.0381	1039	52707	42	10.53	1.5089	6.44	0.0189	0.0397	2.5848
EAS11	242.585358	41.854881	0.0395	1170	52756	189	10.74	1.5299	10.55	0.0765	0.0583	6.6460
EAS12	243.375778	51.059879	0.0336	623	52051	209	10.01	1.1354	18.20	0.0314	0.2572	1.3772
EAS13	246.760666	43.476093	0.0462	815	52374	586	10.95	1.4548	11.41	0.0860	0.0101	7.2333
EAS14	316.286133	−5.399832	0.0826	637	52174	584	11.31	1.5036	9.68	0.4120	0.0396	4.3280
EAS15	343.778320	0.977756	0.0533	379	51789	579	10.83	1.3498	9.70	0.1697	0.5866	4.0352

Notes.
[a] SDSS spectra identification from DR7 (Abazajian et al. 2009).
[b] MPA-JHU Stellar Masses, method described in Brinchmann et al. (2004).
[c] $D_n(4000)$ from SDSS spectra.
[d] Petrosian 90% size in r band, from SDSS photometry.
[e] Limit on SFR from Hα measurements, before aperture correction. Conversion from Kennicutt et al. (1994), line fluxes from MPA-JHU catalogs (Aihara et al. 2011). See Section 2.4.
[f] Limit on SFR from $D_n(4000)$ measurements, from MPA-JHU catalogs (Brinchmann et al. 2004), before aperture correction. See Section 2.5.
[g] Aperture correction to convert fiber-based SFRs to global SFRs, from MPA-JHU catalogs (Brinchmann et al. 2004). See Section 2.5.

Table 2
IRAM 30 m CO(1–0) Observations

Target[a]	t_{obs} (hr)	I_{CO}[b] (K km s^{-1})	L'_{CO}[c] (10^7 K km s^{-1} pc^2)	$M(H_2)$[d] (10^7 $M_\odot$)	FWHM[e] (km s^{-1})
EAH01	0.30	2.58 ± 0.33	128.6 ± 16.4	514.5 ± 65.7	309.8 ± 18.4
EAH02	0.31	1.32 ± 0.27	84.3 ± 17.4	337.0 ± 69.7	172.9 ± 29.8
EAH03	0.20	3.60 ± 0.39	158.0 ± 17.2	632.1 ± 68.9	158.7 ± 8.6
EAH04	0.51	0.59 ± 0.13	9.2 ± 2.0	36.7 ± 7.9	106.7 ± 20.3
EAH05	0.60	0.97 ± 0.21	90.7 ± 19.5	362.7 ± 77.9	278.7 ± 44.8
EAH06	0.71	<0.59	<24.84	<99.34	···
EAH07	1.02	<0.33	<10.31	<41.25	···
EAH08	0.83	0.45 ± 0.15	35.6 ± 12.0	142.5 ± 47.8	233.7 ± 56.9
EAH09	0.61	0.43 ± 0.13	7.8 ± 2.4	31.4 ± 9.7	119.5 ± 28.5
EAH10	0.43	0.73 ± 0.20	181.5 ± 48.6	726.1 ± 194.3	275.1 ± 58.8
EAH11	0.40	<0.60	<38.53	<154.12	···
EAH12	0.70	<0.44	<65.87	<263.47	···
EAH13	0.94	0.68 ± 0.13	193.8 ± 37.6	775.2 ± 150.3	190.1 ± 27.8
EAH14	0.80	<0.53	<44.96	<179.85	···
EAH15	0.60	<0.75	<27.57	<110.27	···
EAH16	0.30	<0.56	<155.85	<623.40	···
EAH17	0.43	<0.51	<25.67	<102.66	···
EAS01	0.33	<0.76	<6.23	<24.93	···
EAS02	0.40	1.11 ± 0.34	12.8 ± 3.9	51.2 ± 15.5	162.7 ± 44.0
EAS03	0.47	1.66 ± 0.24	143.6 ± 21.1	574.4 ± 84.5	270.5 ± 30.3
EAS04	1.56	<0.28	<1.38	<5.51	···
EAS05	0.74	0.64 ± 0.20	30.5 ± 9.5	121.8 ± 38.2	346.9 ± 82.0
EAS06	0.31	3.83 ± 0.39	42.6 ± 4.3	170.6 ± 17.2	112.9 ± 4.0
EAS07	0.61	<0.47	<10.82	<43.27	···
EAS08	1.14	<0.28	<10.06	<40.24	···
EAS09	0.54	2.12 ± 0.27	33.3 ± 4.3	133.3 ± 17.2	267.8 ± 20.5
EAS10	0.80	<0.49	<15.53	<62.12	···
EAS11	0.40	<0.51	<17.20	<68.80	···
EAS12	1.10	0.36 ± 0.12	8.7 ± 2.8	34.9 ± 11.3	141.7 ± 29.1
EAS13	0.39	<0.70	<32.75	<131.01	···
EAS14	1.61	0.83 ± 0.17	124.6 ± 25.3	498.5 ± 101.1	428.7 ± 73.4
EAS15	0.74	0.48 ± 0.15	29.9 ± 9.5	119.8 ± 38.0	166.2 ± 57.2

Notes.
[a] Lines in **bold** represent $>3\sigma$ detections in IRAM 30 m CO(1–0) observations.
[b] Upper limits are shown at the 3σ level.
[c] Calculated using $L'_{CO} = 23.5\ \Omega_b\ D_L^2\ I_{CO}\ (1+z)^{-3}$.
[d] Masses calculated assuming $\alpha_{CO} = 4\ M_\odot\ (\mathrm{K\,km\,s^{-1}\,pc^2})^{-1}$, $M(H_2) = \alpha_{CO} L'_{CO}$.
[e] FWHM from Gaussian fit to data.

[−1200, −400] and [400, 1200] km s^{-1} to fit first order polynomials for baseline subtraction. The spectra are coadded weighted by the rms noise of each scan. The on-source time (T_{ON}) ranges from 12 to 100 minutes depending on the strength of the line toward the targets. If the source was not detected within 3 hr at the telescope ($T_{ON} \approx 1$ hr), we moved on to the next target. The resulting rms noise per 5 km s^{-1} bin is 1.1–4.4 mK and 1.9–9.7 mK for the CO(1–0) and CO(2–1) observations, respectively (T_A^* scale). The conversion factors from K (T_A^* scale) to Jy at our observed frequencies are ∼7.7 Jy K^{-1} and ∼6.0 Jy K^{-1} for the 1.3 mm and 3 mm bands, respectively. We summarize the IRAM 30 m CO observations in Tables 2 and 3 and show the CO spectra in Figures 1 and 2.

2.3. SMT CO Observations

Observations at the SMT 10 m telescope were performed over four runs in 2011 May, 2012 February, 2012 December, and 2013 February. We used the 1 mm ALMA Band 6 dual polarization sideband separating SIS (superconductor–insulator–superconductor) receiver and 1 mHz filterbank to measure the CO(2–1) 230.5 GHz (redshifted to 207.1–227.1 GHz for our sample) line for 13 post-starburst galaxies. The beam size of the SMT for this line is ≈33″. Beam switching was done with the secondary at 2.5 Hz and a throw of 120″. Calibration using a hot load and the standard chopper wheel method was performed every 6 minutes. Calibration using a cold load was performed at every tuning.

To reduce the data, we again use CLASS. The main beam efficiency η_{mb} is calculated using Jupiter in each polarization. We subtract a first-order polynomial baseline from the spectrum using data between [−500, 500] km s^{-1}, excluding the central region of [−300, 300] km s^{-1}. The spectra are scaled using η_{mb}, and coadded, weighting each spectra by the rms noise. We rebin the spectra by a factor of 10, to achieve ≈14 km s^{-1} velocity bins. Typical rms per 14 km s^{-1} channel is 1 mK. We summarize these observations in Table 3 and show the CO spectra in Figures 1 and 2.

2.4. Galaxy Properties from the SDSS

We use a variety of data products from the SDSS to study properties of the post-starburst sample, including emission line fluxes, stellar masses, SFRs, and BPT classifications from the MPA-JHU group catalogs (described in Aihara et al. 2011). We use Petrosian (Petrosian 1976) optical sizes measured in

Table 3
IRAM 30 m and SMT CO(2–1) Observations

Target	t_{obs}[a] (hr)	I_{IRAM}^{2-1}[b] (K km s^{-1})	IRAM 30 m FWHM[c] (km s^{-1})	t_{obs}[d] (hr)	I_{SMT}^{2-1}[b] (K km s^{-1})	SMT FWHM[c] (km s^{-1})	θ_s[e] (arcsec)
EAH01	0.30	4.67 ± 0.57	337.7 ± 18.4	3.10	1.12 ± 0.27	275.7 ± 31.2	$14.6^{+2.9}_{-4.7}$
EAH02	0.26	1.39 ± 0.46	81.6 ± 18.2	...	...	...	...
EAH03	0.20	5.60 ± 0.61	144.0 ± 6.3	2.85	0.64 ± 0.15	149.5 ± 25.2	$3.4^{+3.9}_{-0.7}$
EAH04	0.41	1.51 ± 0.23	125.3 ± 17.0	6.60	0.20 ± 0.03	126.5 ± 16.9	$6.3^{+2.4}_{-2.6}$
EAH05	0.54	1.21 ± 0.30	266.4 ± 54.0	6.00	<0.72	...	...
EAH06	0.71	<1.53	...	...	...	...	...
EAH07	1.03	<0.48	...	...	...	...	...
EAH08	0.76	<1.06	...	3.80	<0.18	...	...
EAH09	0.61	0.78 ± 0.18	127.0 ± 24.2	9.50	<0.20	...	...
EAH10	0.43	<1.83	...	...	...	...	...
EAH11	0.40	<0.66	...	...	...	...	...
EAH12	0.70	<1.15	...	...	...	...	...
EAH13	0.94	<1.17	...	...	...	...	...
EAH14	0.80	<0.98	...	...	...	...	...
EAH15	0.60	<1.14	...	...	...	...	...
EAH16	0.32	<2.05	...	...	...	...	...
EAH17	0.43	<1.69	...	...	...	...	...
EAS01	0.34	<0.81	...	...	...	...	...
EAS02	0.40	2.31 ± 0.70	202.2 ± 62.5	4.60	0.38 ± 0.09	131.2 ± 16.9	$9.0^{+4.1}_{-4.7}$
EAS03	0.47	1.84 ± 0.43	71.0 ± 18.0	6.80	<0.28	...	...
EAS04	1.61	<0.47	...	...	...	...	...
EAS05	0.75	<0.81	...	4.60	<0.77	...	...
EAS06	0.31	5.19 ± 0.54	117.6 ± 3.6	1.50	2.10 ± 0.21	111.7 ± 8.0	$24.0^{+2.1}_{-4.5}$
EAS07	0.61	<0.74	...	...	...	...	...
EAS08	1.00	<0.61	...	...	...	...	...
EAS09	0.55	3.39 ± 0.39	276.1 ± 13.8	2.60	0.79 ± 0.26	234.6 ± 46.3	$13.9^{+4.2}_{-5.2}$
EAS10	0.80	<0.82	...	...	...	...	...
EAS11	0.39	<0.52	...	...	...	...	...
EAS12	1.10	0.62 ± 0.14	...	5.55	<0.27	...	...
EAS13	0.44	<0.81	...	...	...	...	...
EAS14	1.61	1.15 ± 0.30	598.1 ± 199.7	...	...	...	...
EAS15	0.70	1.04 ± 0.22	299.0 ± 58.1	4.50	<0.16	...	...

Notes.
[a] Time on source (hours) IRAM 30 m.
[b] Upper limits are shown at the 3σ level.
[c] FWHM from Gaussian fit to data.
[d] Time on source (hours) SMT.
[e] Approximate Gaussian source size (FWHM) of CO emitting region, see text (Section 4.2) for details.

the r band from the SDSS photometric catalogs, and redshifts from DR7.

We use the stellar masses calculated from the SDSS spectra (method described in Kauffmann et al. 2003a; Salim et al. 2007) and included in the MPA-JHU data products. Because the star formation histories of post-starbursts may not be well represented by the templates assumed in the spectral fitting, we estimate the systematic error by comparing stellar masses from several different algorithms run on SDSS data. We compare the stellar masses from the MPA-JHU data products to those calculated by Chen et al. (2012), who use both the Bruzual & Charlot (2003) and Maraston & Strömbäck (2011) SPS models. All three stellar mass calculations use a Kroupa initial mass function (IMF). The systematic error from this method slightly exceeds the formal errors on the MPA-JHU measurements and is typically ~30%.

2.5. Star Formation Rate Upper Limits

We use two different methods to calculate SFRs for the post-starburst sample, one employing the Hα luminosity and the other the $D_n(4000)$ break. Both are contaminated by other effects (principally LINER and A-stellar emission, see below), and serve as upper limits on the actual current SFR.

Using the emission line fluxes from the MPA-JHU data set (Aihara et al. 2011), we calculate SFR limits from Hα luminosities using the relation from Kennicutt et al. (1994). We use the Balmer decrement of Hα/Hβ to calculate dust extinction, assuming the standard case B recombination at $T = 10^4$ K and an intrinsic value of 2.86. We use the reddening curve of O'Donnell (1994). For the cases where the Hβ line flux is uncertain, we use the mean value of $E(B-V)$ of the other post-starburst galaxies. The mean attenuation is then $A_V = 0.92$ mag, or $A_{H\alpha} = 0.77$ mag.

A complicating factor in determining the SFRs from Hα for the post-starburst sample is the high incidence of LINER spectra. A BPT diagram for the post-starburst sample is shown in Figure 3. Two galaxies lie in the transition region, and the rest are categorized as LINERs. Although the source of the LINER may not be an AGN (LINER emission is commonly seen in late stage mergers: Rich et al. 2011, and from post-asymptotic giant branch stars: Singh et al. 2013), processes in addition to star formation will contribute to nebular line fluxes here, making the derived SFRs upper limits.

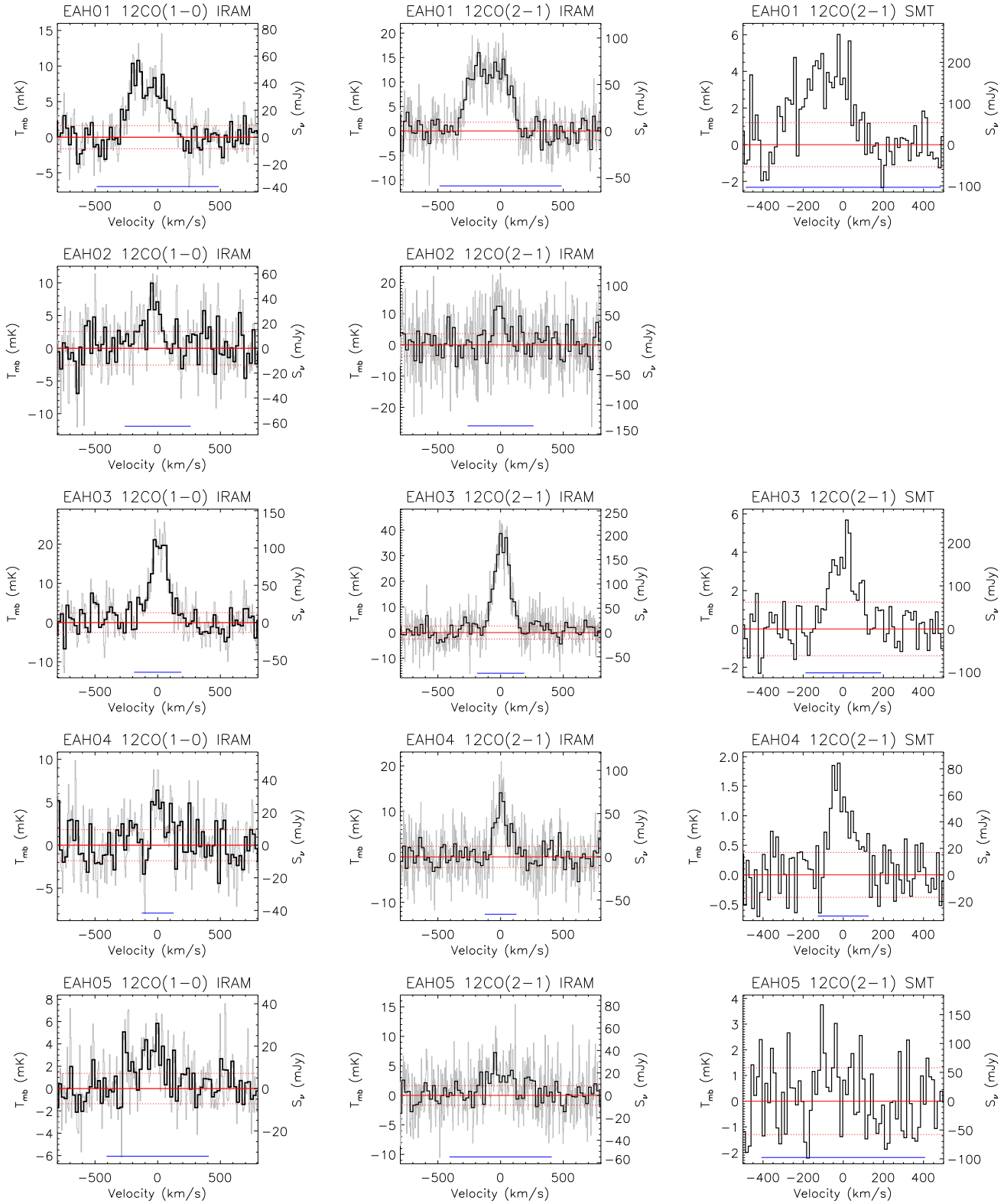

Figure 1. CO(1–0) and CO(2–1) spectra from IRAM and SMT for galaxies with IRAM-30 m CO(1–0) detections ($>3\sigma$) in our post-starburst sample. Spectra are shown in units of both main beam temperature $T_{\rm mb}$ (mK) and S_υ (Jy). Gray lines show the unbinned IRAM data for 5 km s^{-1} channels, and black lines show the data binned to 20 km s^{-1}. Dashed red lines represent the rms of the binned data. SMT data are shown in 13 km s^{-1} bins. Blue horizontal lines at bottom represent the integration intervals, as described in the text.

The MPA-JHU group use the $D_n(4000)$ break as a less precise, but less contaminated way to estimate SFRs when galaxies do not lie in the star-forming sequence on the BPT diagram (Brinchmann et al. 2004). The $D_n(4000)$ break is a measure of the specific SFR (sSFR), and is calculated from regions of the rest-frame spectra bracketing the strong "break" observed near 4000 Å. $D_n(4000)$ is not expected to be influenced by the presence of a Type II AGN (Kauffmann et al. 2003b). The conversion between $D_n(4000)$ and sSFR is calibrated from those galaxies in the SDSS categorized as star-forming. The scatter in

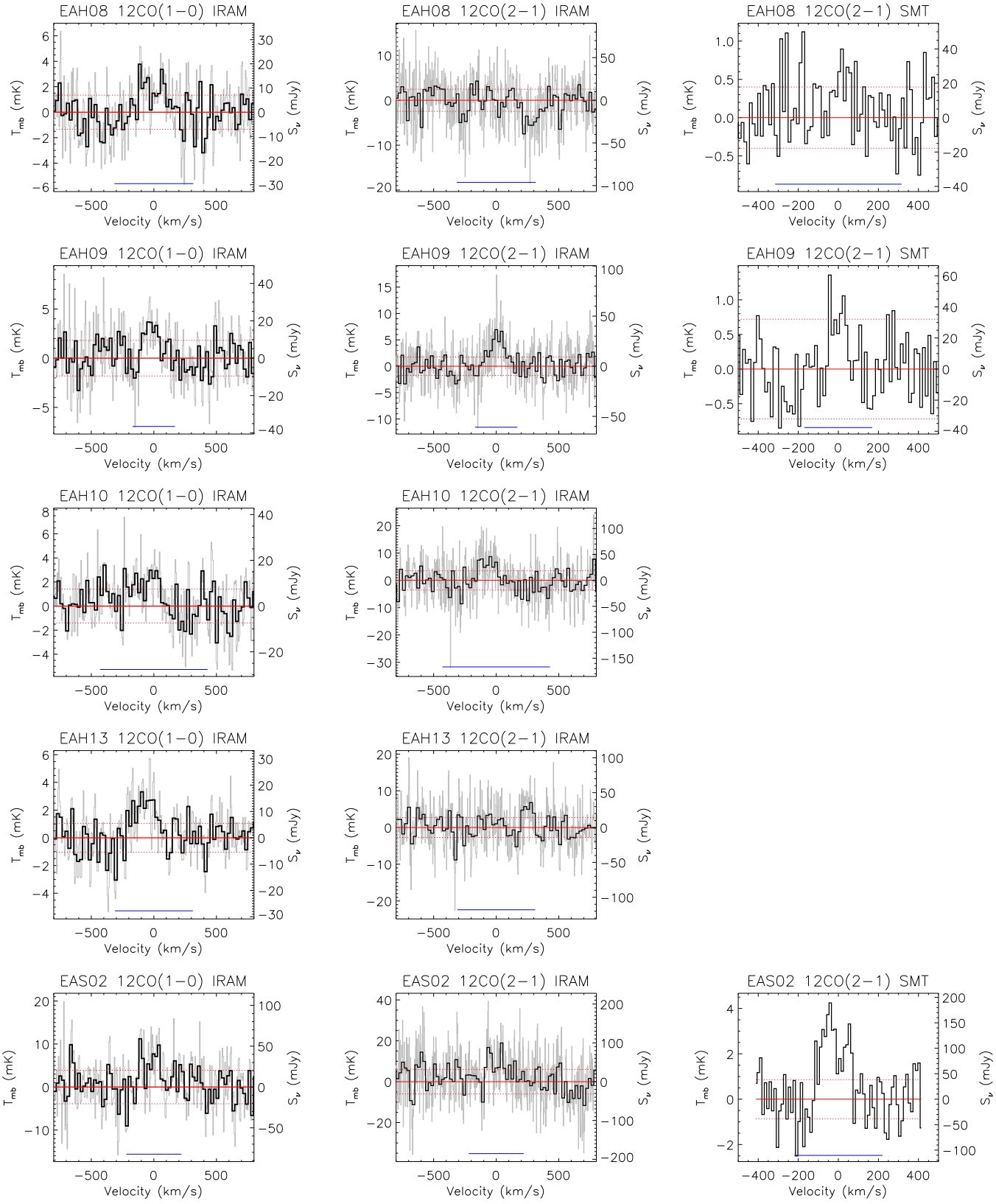

Figure 1. (Continued)

this relation is large, and the error bars we show on the $D_n(4000)$ SFRs (derived using the MPA-JHU stellar masses) reflect the low precision of this calibration.

The problem with using the $D_n(4000)$-based SFRs in post-starburst galaxies is their sensitivity to the bright A-stellar populations produced in the recent burst. During ongoing star formation, the 4000 Å break is minimal, so $D_n(4000)$ is low. In passive galaxies, $D_n(4000)$ is large. However, the timescale over which $D_n(4000)$ is affected by a strong burst (∼1 Gyr; see, e.g., Kauffmann et al. 2003a) is larger than the

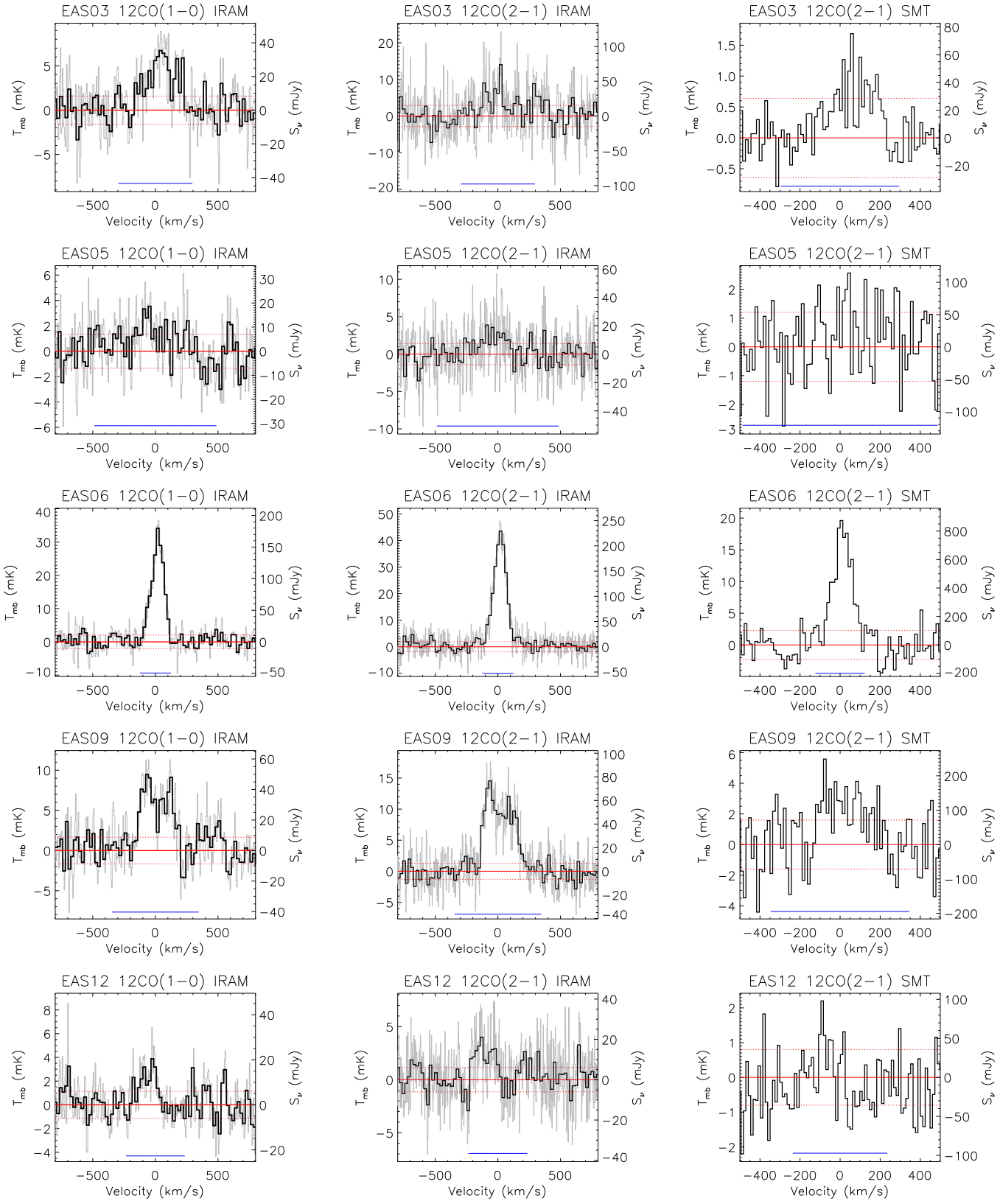

Figure 1. (Continued)

post-burst ages of our sample, so $D_n(4000)$ here will reflect both previous and current rates of star formation. $D_n(4000)$ will be lower (more like star-forming galaxies) in post-starbursts than expected given their instantaneous SFRs. Lower values of $D_n(4000)$ correspond to higher SFRs, so $D_n(4000)$ will overestimate the current SFR due to the recent burst. We use $D_n(4000)$-based SFRs as upper limits on the current SFR.

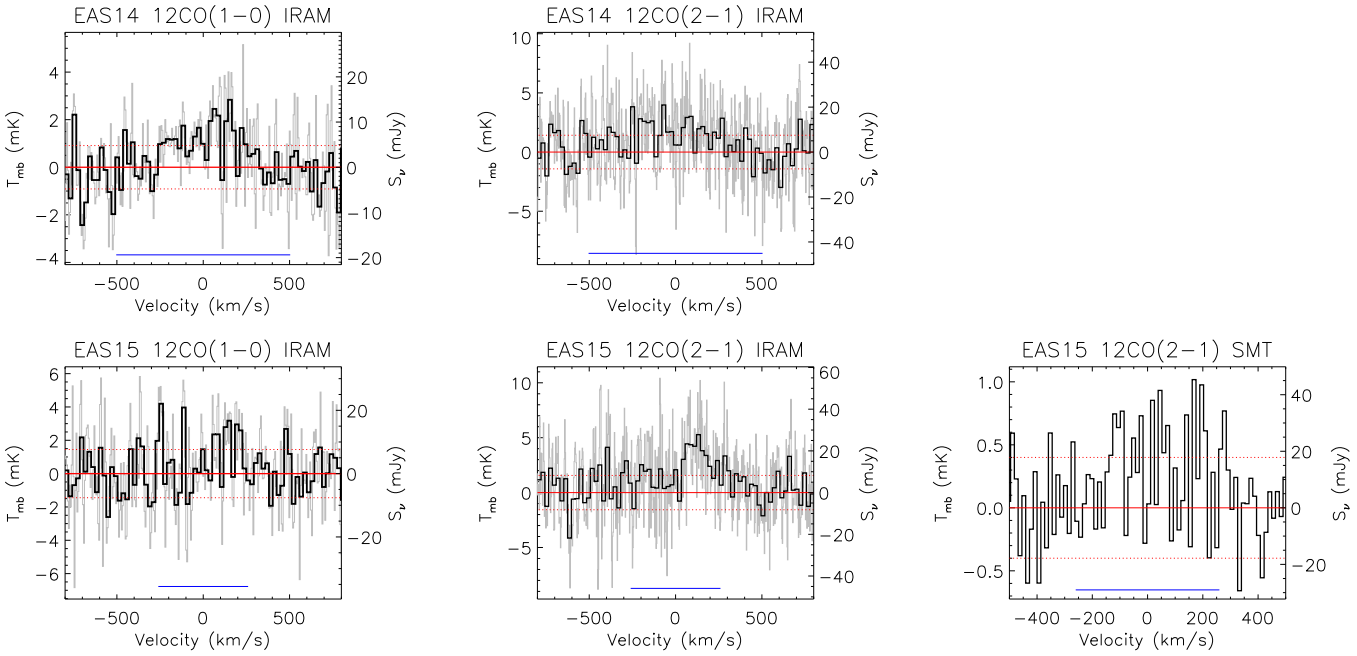

Figure 1. (Continued)

To use the SDSS fiber spectra to calculate global SFRs, we must account for any star formation outside the 3″ fiber aperture. Like Brinchmann et al. (2004), we see a trend of increasing fiber-based SFR per total stellar mass with redshift, after breaking up our complete SDSS post-starburst sample (1207 galaxies) into stellar mass bins. Thus, we expect some contribution to the SFR from outside of the fiber, so we require an aperture correction.[9] We apply the aperture correction used in the MPA-JHU SFRs (Brinchmann et al. 2004; Salim et al. 2007; Aihara et al. 2011), which is based on galaxy photometry outside the fiber. Although this aperture correction is calibrated on star-forming galaxies, it successfully removes the trend of sSFR with redshift for our complete post-starburst sample. While our use of this correction assumes that it also applies to our post-starbursts, the corrected SFRs remain likely upper limits as post-starbursts tend to have more positive color gradients (relatively bluer cores) than star-forming galaxies (Yang et al. 2006, 2008).

One case where Hα and $D_n(4000)$ would not provide upper limits on the SFRs is if we have significantly underestimated the dust extinction in post-starbursts. Radio continuum emission at 1.4 GHz is often used as an "extinction-free" SFR indicator (Condon 1992). We search the Faint Images of the Radio Sky at Twenty centimeters (FIRST; Becker et al. 1995) and NRAO VLA Sky Survey (NVSS; Condon et al. 1998) 1.4 GHz surveys for matches within 10″ of each galaxy in our sample. We find six detections in the FIRST survey (S06, H01, H03, H07, H08, and H09). The galaxies H07, H08, and H09 are also detected in the NVSS. Using the conversion found in Condon (1992), the SFRs suggested by these detections are higher than the Hα SFRs. If we were to accept that the standard 1.4 GHz–SFR relation is valid for the post-starburst sample, it would require these galaxies to have up to 4.7 mag of additional extinction on top of the ∼1 mag already accounted for using the Balmer decrement. While dust extinctions of 5–6 mag are not unheard of, especially for starbursts, the dust extinction is consistent with that implied by Balmer decrement in those cases (Choi et al. 2006; Kennicutt et al. 2009). The huge difference between the extinction derived from the Balmer decrement and implied by the 1.4 Ghz–SFR relation is unprecedented and suggests a problem with the SFRs derived from the 1.4 GHz data for our post-starbursts.

The LINER and recent starburst in these galaxies complicate the standard 1.4 GHz SFR conversion. Galaxies with LINER spectra have enhanced 1.4 GHz fluxes when compared to other measures of their SFRs (de Vries et al. 2007; Morić et al. 2010). Morić et al. (2010) find that 90% of the 1.4 GHz flux can come from the LINER, not from star formation, and that the scatter in the 1.4 GHz–SFR relation for LINERs is large, of order 2 dex. For our sample, the 1.4 GHz-based SFRs and limits scatter evenly about the Hα-based SFRs after the radio SFRs are reduced by the expected factor of 10. While the LINER will also contribute to the Hα flux, its contribution is typically $\lesssim$40%, with less scatter (Brinchmann et al. 2004), implying that Hα is more reliable than 1.4 GHz as a SFR upper limit. Additionally, the recent large starburst may boost the amount of 1.4 GHz flux on timescales overlapping with the post-burst ages of our sample (Bressan et al. 2002). As discussed above in Section 2.1, the galaxies marked "S" were selected with a cut on the [O III] EWs, intended to exclude galaxies with strong AGN activity from the sample. This cut was not applied to the selection of galaxies marked "H," and the higher incidence of 1.4 GHz detections in the "H" sample may be tied to a higher incidence of AGN.

Both the TIR luminosity (total IR, from 8–1000 μm; Hayward et al. 2014) and 24 μm flux (Utomo et al. 2014) are strongly affected by dust heating by the substantial A stellar population in post-starbursts, so we do not consider these SFR indicators here. Ongoing analysis of our sample observed in polycyclic aromatic hydrocarbon (PAH) emission and high ionization species (A. Smercina et al., in preparation) will provide further constraints on any current SFR.

In the following analysis, we use the Hα-derived SFR as an upper limit, as well as showing the effect of assuming the $D_n(4000)$-based SFRs.

[9] We consider the case where star formation is limited to the fiber aperture in Section 4.2, see Figure 11 (right).

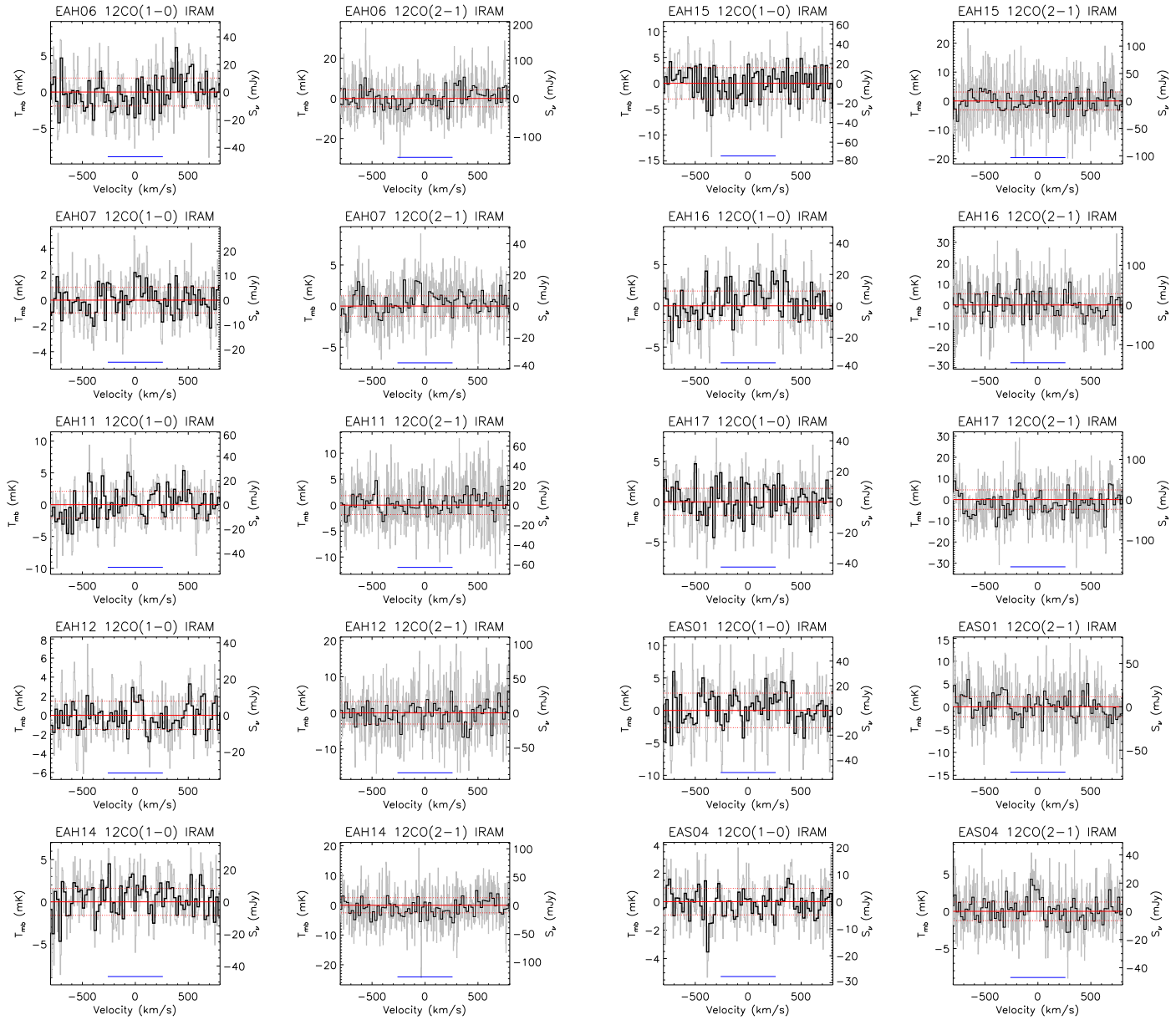

Figure 2. CO(1–0) and CO(2–1) spectra from IRAM and SMT for galaxies with CO(1–0) not detected with the IRAM 30 m. Spectra are shown in units of both main beam temperature $T_{\rm mb}$ (mK) and S_ν (Jy). Gray lines show the unbinned IRAM data for 5 km s^{-1} channels, and black lines show the data binned to 20 km s^{-1}. Dashed red lines represent the rms of the binned data. SMT data are shown in 13 km s^{-1} bins. Blue horizontal lines at bottom represent the integration intervals, as described in the text.

Figure 2. (Continued)

3. RESULTS

3.1. Detection of Molecular Gas

We detect molecular gas at $>3\sigma$ in 17 of the 32 galaxies observed, using IRAM 30 m measurements of the CO(1–0) line. If we increase our detection threshold to 4σ, we detect 14 galaxies, and at $>5\sigma$, we detect 11 galaxies. To calculate the integrated CO line intensity $I_{\rm CO}$, we fit a Gaussian profile to each line, allowing the center velocity to differ from the optical velocity up to 200 km s^{-1}. We use the Gaussian width $\sigma_{\rm gauss}$ to choose integration limits of $\pm 3\sigma_{\rm gauss}$. Although many of the line shapes are not exactly Gaussian, this method allows us to estimate appropriate velocity intervals for integration in a systematic way. FWHMs given by these fits are listed in Tables 2 and 3. If the S/N for $\sigma_{\rm gauss}$ is <3, we use the interval [−260, 260] km s^{-1} These velocity limits were chosen to be the median of those of the well-fit sample, and are centered around the optical velocity. The velocity intervals fit from the CO(1–0) data are used for the CO(2–1) data, though we note that fitting the CO(2–1) data separately does not change our results by $>1\sigma$. We calculate the error in the integrated CO line intensity as

$$\sigma_I^2 = (\Delta v)^2\, \sigma^2\, N_l \left(1 + \frac{N_l}{N_b}\right), \quad (1)$$

where Δv is the channel velocity width, σ is the channel rms noise, N_l is the number of channels used to integrate over the line, and N_b is the number of channels used to fit the baseline. We also take into account an estimated flux calibration error of 10%. We calculate upper limits on $I_{\rm CO}$ as $<3\sigma_I$. Following Solomon et al. (1997), the CO line luminosity $L'_{\rm CO}$ (in K km s^{-1} pc^2) is

$$L'_{\rm CO} = 23.5\, \Omega_{s*b}\, D_L^2\, I_{\rm CO}\, (1+z)^{-3}, \quad (2)$$

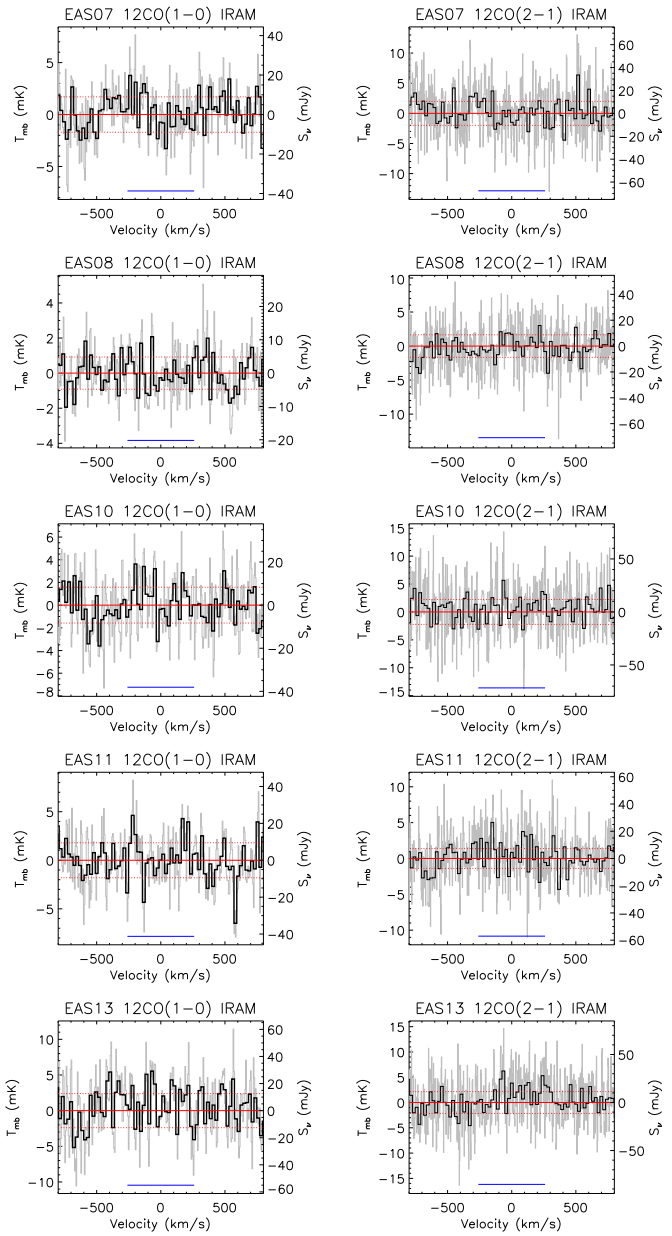

Figure 2. (Continued)

where $I_{\rm CO} = \int T_{\rm mb}\, dV$ is the integrated line intensity (in K km s^{-1}) as described above, z is the SDSS redshift, and D_L is the luminosity distance (in Mpc). Ω_{s*b} is the solid angle of the source convolved with the beam,

$$\Omega_{s*b} = \frac{\pi\left(\theta_s^2 + \theta_b^2\right)}{4\ln 2}, \quad (3)$$

where θ_s and θ_b are the half power beam widths of the source and beam, respectively. Because the CO emitting size estimates (see Section 4.2) are not available for all the sources, we adopt a simple approximation such that the beam is much larger than the source, so $\Omega_{s*b} \approx \Omega_b$. Note that depending on the actual size estimates in Section 4.2, we could be underestimating $L'_{\rm CO}$ by ∼1.1–2.2×, with a median of 1.4, but this does not affect our conclusions throughout the paper.

The molecular gas mass can be calculated from $L'_{\rm CO}$ by assuming a conversion factor $\alpha_{\rm CO}$, as

$$M({\rm H_2}) = \alpha_{\rm CO} L'_{\rm CO}. \quad (4)$$

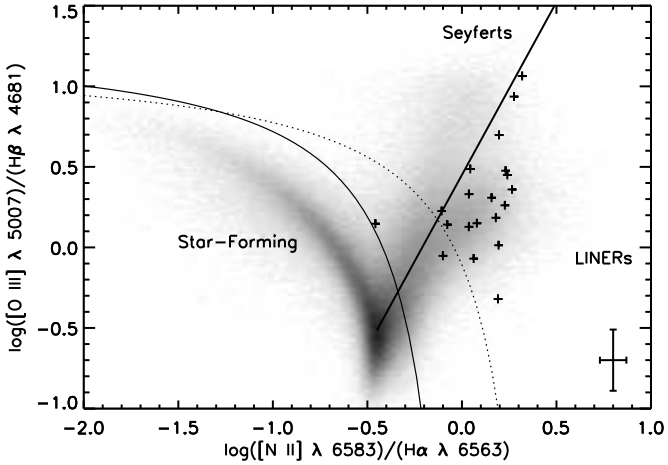

Figure 3. BPT (Baldwin et al. 1981) diagram for post-starburst sample, measured from SDSS spectra. Galaxies from the SDSS DR7 (Abazajian et al. 2009) with well-measured lines are shown as a shaded background. The lines separating star-forming and AGN-like activity from Kewley et al. (2001) and Kauffmann et al. (2003b) are shown as dotted and solid lines, respectively. The line at $\Phi = 25°$ separates Seyferts from LINERs. The post-starburst sample is plotted as individual points, for galaxies with all lines detected at $>3\sigma$, with a characteristic errorbar shown in the bottom right. Most of the post-starburst sample, except S12, is solidly in the LINER category. The presence of LINERs complicates our calculation of the current SFR, as the nebular emission lines will be contaminated.

For now, we assume an $\alpha_{\rm CO}$ comparable to that in Galactic molecular clouds and the Local Group (aside from the Small Magellanic Cloud; see recent reviews by Bolatto et al. 2013; Carilli & Walter 2013; Casey et al. 2014): $\alpha_{\rm CO} = 4\ M_\odot$ (K km s^{-1} pc^2)$^{-1}$ (units omitted hereafter). This choice is examined below and in Section 4.3.

Molecular gas masses for the post-starburst sample span a broad range, from 3.4×10^8 to $6.9 \times 10^9 M_\odot$, with a mean value of $3.0 \times 10^9 M_\odot$ among the detected sample. We measure upper limits for the remaining 15 galaxies, with 3σ limits ranging from 4.6×10^7 to $5.2 \times 10^9 M_\odot$. Molecular gas masses and upper limits are listed in Table 2. Optical postage stamps of the galaxies with and without molecular gas detections are shown in Figures 4 and 5, respectively.

Next, we compare the molecular gas masses measured here to those from surveys of other galaxy types. CO(1–0) measurements have been compiled for the Atlas-3D sample of early type galaxies (Young et al. 2011). The COLD GASS (Saintonge et al. 2011) sample is a stellar mass-limited sample of galaxies, selected from the SDSS independent of galaxy type. We divide the COLD GASS sample up by galaxy type assigned by the SDSS based on the optical spectra (galspec `bptclass`). For now, we only use galaxies classified as star-forming or low S/N star-forming. We assume $\alpha_{\rm CO} = 4$ to calculate molecular gas mass for the early type and COLD GASS star-forming samples.

We compare the total molecular gas masses of these samples in Figure 6, seeing significant overlap between the star-forming and post-starburst samples. This overlap is surprising, because of the lack of equivalent levels of current star formation in the post-starburst sample. The lower mass end, as well as the upper limits, of the post-starburst sample are consistent with the early type sample.

In addition to comparing $M({\rm H_2})$, we also compare molecular gas fraction $f_{\rm gas} \equiv M({\rm H_2})/M_\star$ normalized by stellar mass $M_\star$. We use $M_\star$ calculated from the SDSS spectra, as discussed in Section 2.4, for both the post-starburst and COLD GASS

Figure 4. 60″ by 60″ SDSS postage stamps of the 17 post-starburst galaxies with CO(1–0) detected at $>3\sigma$ with the IRAM 30 m. The size of the 3″ SDSS fiber is overplotted in blue, and the size of the IRAM 30 m CO(1–0) 22″ beam is overplotted in orange. Galaxies are ordered by decreasing $M(H_2)$. Given the size estimates in Section 4.2, we could be underestimating L'_{CO} by factors of ∼1.1–2.2×, with a median of 1.4, due to aperture effects.

samples. We calculate stellar masses for the early type galaxies in the same way as Atlas-3D, using *K*-band measurements (Cappellari et al. 2011).

As with the $M(H_2)$ comparison, we see considerable overlap in f_{gas} between the post-starburst and star-forming samples. These comparisons are shown in the right-hand panels of Figure 6. The molecular gas fractions for the post-starburst sample are primarily above those of the early type sample, while some of the upper limits are more consistent with early types.

The CO to H_2 conversion factor (α_{CO}) is a known source of uncertainty in observations of molecular gas (see recent review by Bolatto et al. 2013). Traditionally, a bimodal model has been used, with normal star-forming galaxies assigned a Milky Way-like value of $\alpha_{CO} \sim 4$, and ultraluminous infrared galaxies (ULIRGs) or starbursting galaxies assigned $\alpha_{CO} \sim 0.8$.

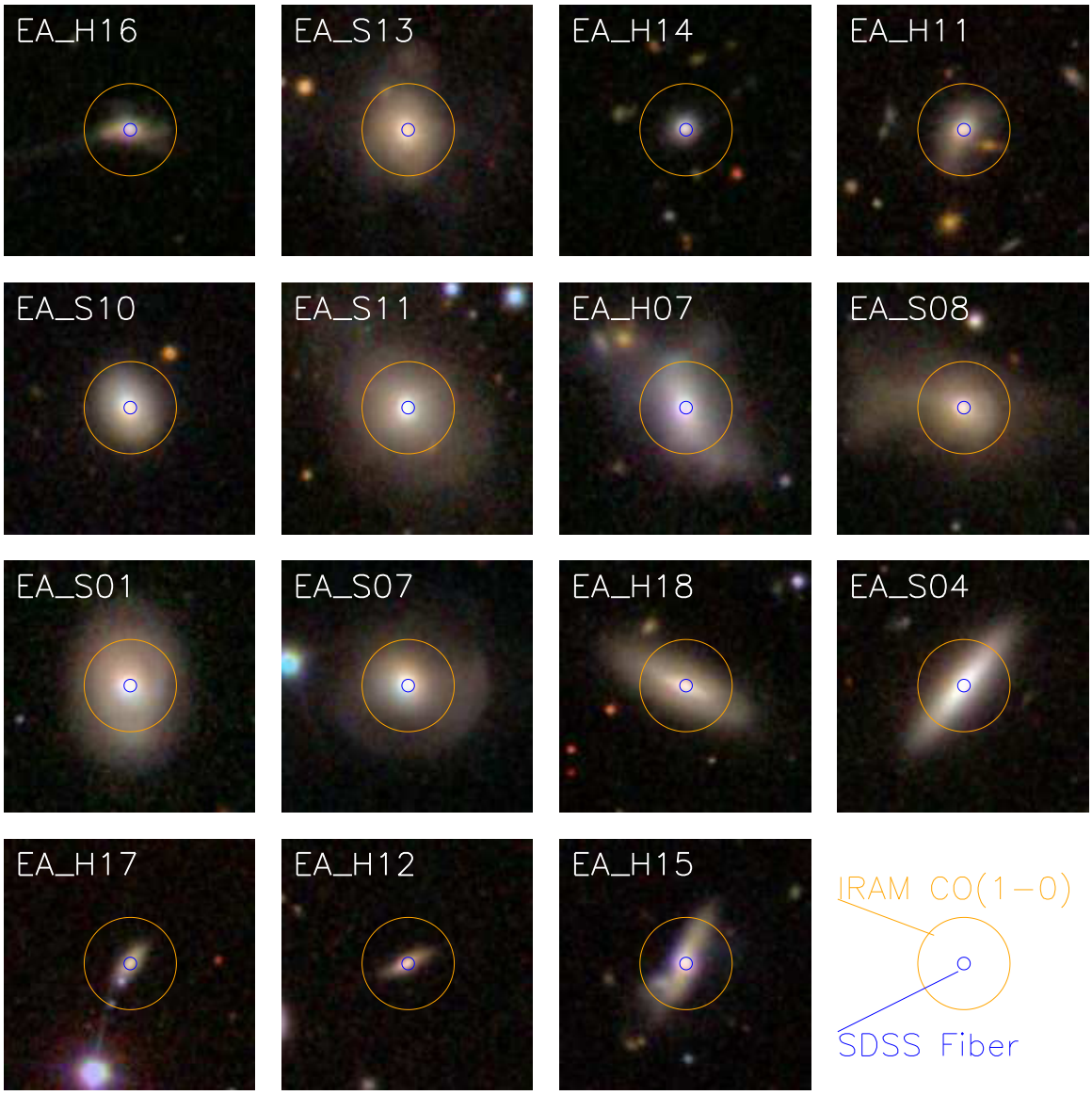

Figure 5. Same as Figure 4, but for the galaxies not detected in CO(1–0).

This approach was initially motivated by the fact that a high α_{CO} applied to ULIRGs produced gas masses higher than the dynamical masses. In Figure 7, we plot $M(H_2)$ and f_{gas} for the post-starbursts and comparison galaxies for different α_{CO} assumptions. We also compare to the sample of luminous infrared galaxies (LIRGs) and ULIRGs from Gao & Solomon (2004). Even if a low, ULIRG-like value of $\alpha_{CO} = 0.8$ is used for the post-starburst sample, we still see significant overlap with the star-forming sample (at $\alpha_{CO} = 4$), and even some overlap with the LIRG and ULIRG sample (at $\alpha_{CO} = 0.8$). We expect $\alpha_{CO} = 0.8$ and $\alpha_{CO} = 4$ to span the range of possible values of α_{CO} in post-starburst galaxies, because recently ended starbursts may reflect interstellar medium (ISM) physical conditions between ULIRGs and quiescent disk galaxies. However, the appropriate value of α_{CO} for post-starbursts remains largely unconstrained. We discuss the effects of this uncertainty on our results in Section 4.3.

3.2. High Molecular Gas Mass for Given SFR

We compare the molecular gas masses measured here to upper limits on SFR derived from Hα and $D_n(4000)$ in Figure 8. We use several comparison data sets: star-forming galaxies selected from the COLD GASS (Saintonge et al. 2011, 2012), the star-forming and starburst sample from Gao & Solomon (2004), and early type galaxies (with Hα+PAH SFRs) from Young et al. (2011) and Davis et al. (2014). The post-starburst sample lies at higher $M(H_2)$ for their SFRs than early-types, star-forming galaxies, and (U)LIRGs. The median Hα-derived SFR upper-limit for the post-starburst sample is $\sim$10$\times$ lower than the median SFR for the COLD GASS star-forming sample across the same $M(H_2)$ range. This offset persists for the median of the $D_n(4000)$-derived SFR upper limits, which is $\sim$20 $\times$ lower than expected given $M(H_2)$.

Is it possible that our post-starburst selection criteria have generated the observed offset in SFR? Because we selected the post-starburst sample to have low Hα EWs, it may include star-forming galaxies whose EW(Hα) measurement errors have scattered them low. This does not appear to be the case, as star-forming galaxies (classified using `bptclass=1`) that pass our Hδ absorption cut typically have EW(Hα) $\gg$ 3 Å, the limit for our post-starburst sample. A Monte Carlo analysis predicts a 0.004% contamination rate, and even if the Hα

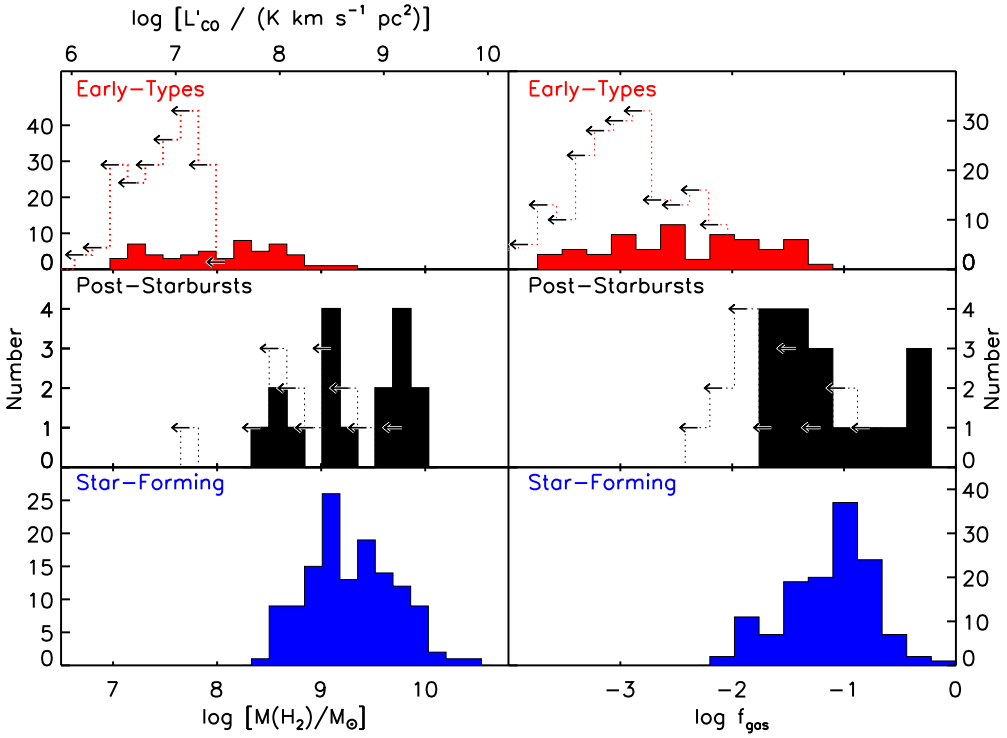

Figure 6. Left: histograms of derived molecular gas masses $M(H_2)$ for a variety of galaxy types: early types (top, from Atlas-3D; Young et al. 2011), star-forming (bottom, from COLD GASS; Saintonge et al. 2011), and our post-starburst sample (middle). $\alpha_{CO} = 4\,M_\odot\ (K\,km\,s^{-1}\,pc^2)^{-1}$ is assumed for all samples. Bin size represents the mean error in the post-starburst sample, excluding systematic error from uncertainties in α_{CO}. A histogram of 3σ upper limits is overplotted for non-detections. Right: histograms of molecular gas normalized to stellar mass (f_{gas}) for the same samples. For both $M(H_2)$ and f_{gas}, we see considerable overlap between the post-starburst sample and star-forming samples, which is surprising given the difference in SFRs. The lower end and upper limits of the post-starburst sample are consistent with $M(H_2)$ and f_{gas} measured for the early type sample. As seen in Figure 7, overlap persists even if a ULIRG-type value of α_{CO} is assumed for the post-starburst sample.

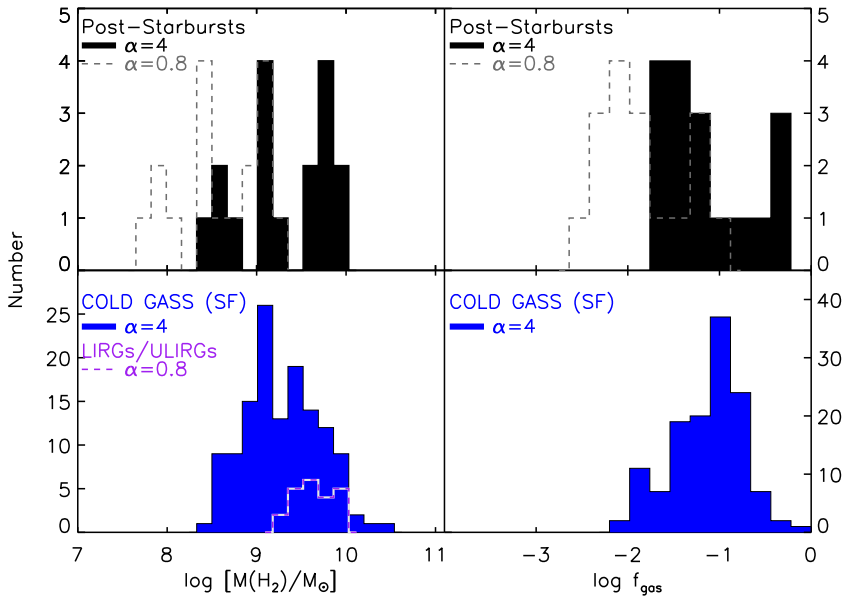

Figure 7. Left: histograms of derived molecular gas masses $M(H_2)$ for a variety of galaxy types: star-forming (bottom, from COLD GASS; Saintonge et al. 2011), LIRGs and ULIRGs (bottom, from Gao & Solomon 2004), and our post-starburst sample (top). $\alpha_{CO} = 4\,M_\odot\ (K\,km\,s^{-1}\,pc^2)^{-1}$ is assumed where data are plotted as solid histograms, and $\alpha_{CO} = 0.8\,M_\odot\ (K\,km\,s^{-1}\,pc^2)^{-1}$ where histograms are dashed lines. Bin size represents the mean error in the post-starburst sample. Right: histograms of molecular gas normalized to stellar mass (f_{gas}) for the same samples (except for Gao & Solomon 2004). Even if a low, ULIRG-like value of α_{CO} is used for the post-starburst sample, we still see significant overlap with the star-forming sample, and even some overlap with the LIRG and ULIRG samples.

EWs had systematic errors 3× as large as their measurement errors, we still expect ≪1 contaminant in the complete SDSS post-starburst sample of 1207 galaxies. Thus, the KS offset does not arise from contamination from normal star-forming galaxies.

The large molecular gas reservoirs in post-starburst galaxies are inconsistent with their SFRs when compared to a broad sample of galaxy types. Thus, the cessation of star formation after the starburst cannot be due to a lack of gas in the nearly half of our sample with detected CO. The question remains:

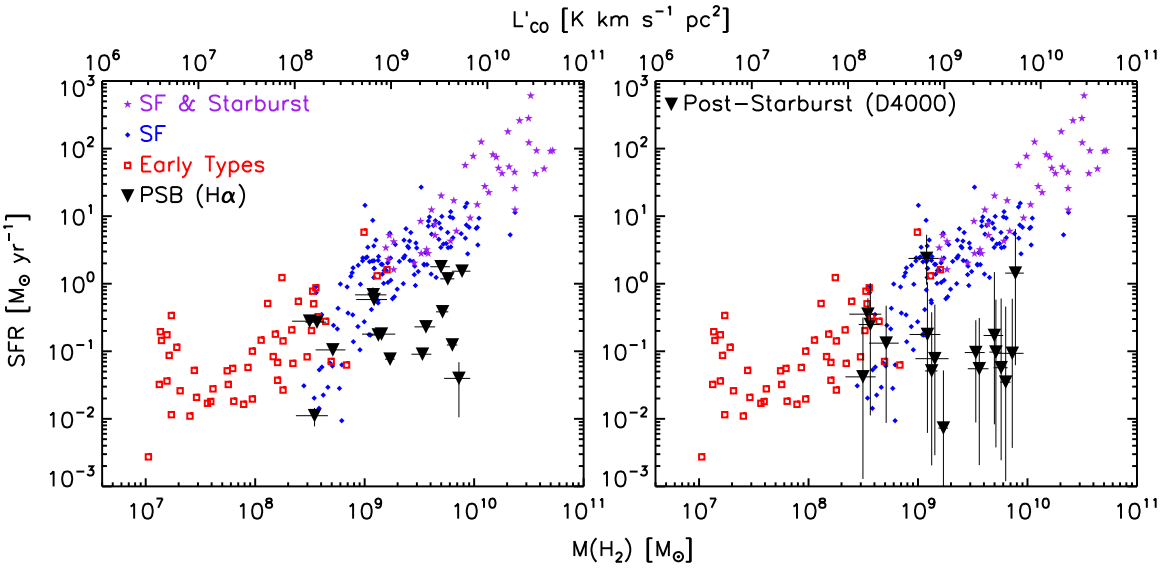

Figure 8. Molecular gas mass vs. SFR for post-starburst (PSB) galaxies and comparisons. Whether Hα (left) or $D_n(4000)$ (right) SFR upper limits are used for the post-starburst sample, these galaxies fall systematically below the comparison galaxies from the COLD GASS sample classed by the SDSS as star-forming (Saintonge et al. 2011, 2012), star-forming, LIRG, and ULIRG galaxies from the Gao & Solomon (2004) sample, and early type galaxies from Young et al. (2011). Both $D_n(4000)$ and Hα are expected to overestimate the SFR in the post-starburst sample, so these galaxies may lie at even lower SFRs. All galaxies have been normalized to the same value of $\alpha_{CO} = 4$.

why are these galaxies no longer forming stars at significant rates? One possibility is that the molecular gas is spread out over a larger area, dropping its surface density to be consistent with SFR density on the KS relation (Kennicutt 1998, hereafter K98). We examine the KS relation below.

3.3. Offset from the Kennicutt–Schmidt Relation

While there are clear trends of SFR with molecular gas mass, tighter correlations exist when comparing the surface densities of these quantities for normal star-forming and starburst galaxies.

We determine the molecular gas surface density Σ_{H_2} and SFR surface density Σ_{SFR} for the post-starburst sample, using the SDSS r-band Petrosian 90% radius to calculate the area as

$$\Sigma_{H_2} = \alpha_{CO} L'_{CO} / (\pi R_{90}^2); \quad \Sigma_{SFR} = SFR / (\pi R_{90}^2). \quad (5)$$

We place the post-starburst sample on a KS plot in Figure 7. Other local galaxies are shown for comparison, including both normal star-forming galaxies and starbursts from the canonical K98 sample. For now, we apply the same value of $\alpha_{CO} = 4$ to the post-starburst sample, and the entirety of the K98 sample. Many of the post-starburst galaxies lie below the relation defined by the other galaxies: the Hα-derived SFR limits exclude consistency with the relation for all but 4–5 galaxies. The $D_n(4000)$ based SFR limits also lie mostly below the relation.

The median locus of the 17 post-starburst galaxies lies $4^{+2}_{-1.5}\times$ lower than the $n = 1.4$ power law fit to the K98 galaxies. We perform a Monte Carlo analysis to assess the significance of this result by choosing random sets of 17 galaxies from the K98 disk sample, finding a 5σ significant offset for the post-starburst locus. This offset is more extreme than that found by Davis et al. (2014) for their sample of gas-rich early type galaxies. The relationship between the two data sets is unclear.

We see no obvious differences between the properties of our galaxies that are roughly consistent and most discrepant with the KS relation. It is not clear if the post-starbursts are single population of galaxies, or several different families.

The optical size used by K98 to calculate the surface densities is the isophotal radius, where the B-band surface brightness drops to 25 mag arcmin^{-2} and which is comparable to the Hα emitting region for normal spiral galaxies (K98, although we test this assumption for our sample in Section 4.2). This isophotal radius should be a good estimate of the size if the CO emission is coming from the same region as the optical light from star formation. Here, we use the Petrosian 90% radius for our post-starbursts, because the isophotal sizes in SDSS are not considered reliable and are not included in the photometric catalogs after DR8. However, the significant offset from the K98 sample remains if we use the r-band isophotal radii instead.

There are several other observational uncertainties that could affect our results, which we consider in Section 4. We discuss the effect of our sample selection criteria in Section 4.1. Like K98, we assume that the optical size of the galaxies is a good proxy for the spatial extent of both star formation and molecular gas. This assumption may not be valid for post-starburst galaxies. In Section 4.2, we test the possibilities that the CO is distributed differently from the optical light and that the star formation is distributed differently from both the optical light and most of the H_2, as traced by CO. We also consider how our sampling of the CO region (aperture bias) might affect our results. In Section 4.3, we test for the possibility that the measured CO is not tracing the H_2 as we expect, resulting in a different α_{CO}.

4. DISCUSSION

4.1. Possible Sample Selection Biases

Given the way we selected our CO targets, the sample observed here might not represent the gas properties of the overall post-starburst sample. To study any biases that may occur within our sample, we test whether the galaxies with CO(1–0) detections lie at the extremes of our selection criteria.

The two parts of our sample (labeled "H" and "S") were selected from the parent sample of SDSS post-starbursts using different criteria (more details in A. Smercina et al., in

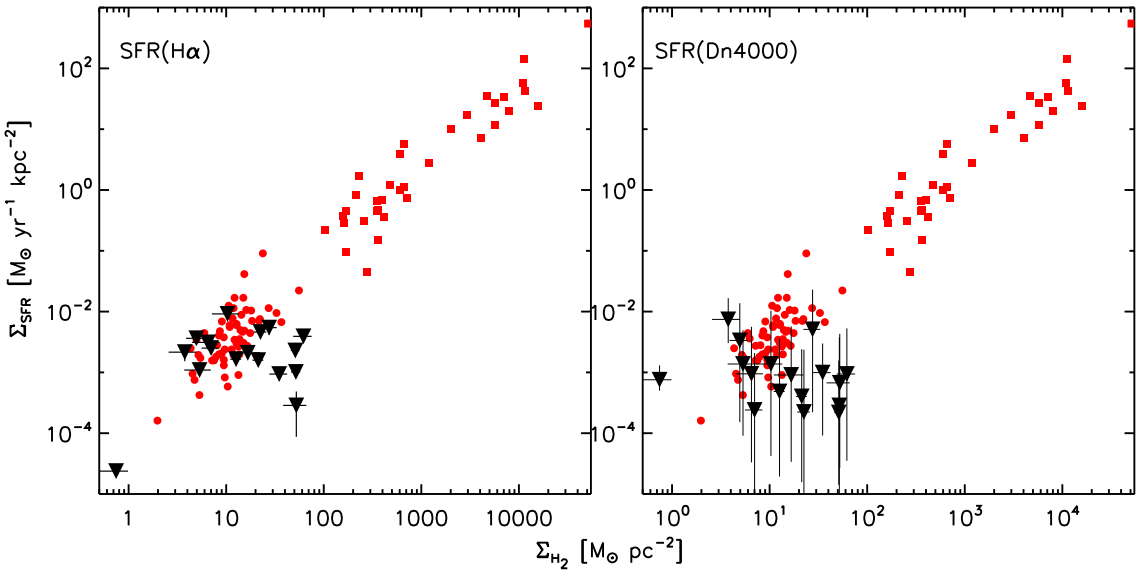

Figure 9. Molecular gas surface density vs. SFR surface density from Hα (left) and $D_n(4000)$ (right) SFR upper limits. The post-starburst sample is shown in black, with other local galaxies (Kennicutt 1998) shown in red. Red circles are normal star-forming galaxies and red squares indicate local starbursts. Both SFR indicators are upper limits to the true current SFRs for the post-starburst sample. Hα has a contribution from the LINER, and $D_n(4000)$ has a contribution from the intermediate age stars produced in the burst. Our post-starburst galaxies are biased low on this relation. For the post-starburst sample, we assume the CO is distributed in the same way as the star formation regions, using the Petrosian 90% radius R_{90} to calculate the surface densities, $\Sigma_{SFR} = SFR/\pi R_{90}^2$ and $\Sigma_{H_2} = M(H_2)/\pi R_{90}^2$. Here, $M(H_2)$ includes all the CO detected in the IRAM 30 m beam. We use the same value of $\alpha_{CO} = 4$ for all galaxies. This plot is the most appropriate comparison to the K98 data set, although we test our assumption that CO and star formation are distributed like the optical light in Section 4.2, and that $\alpha_{CO} = 4$ in Section 4.3.

preparation). The "H" sample was selected based on post-starburst galaxies bright in the *WISE* 12 μm band. One might expect these galaxies to have more gas if the 12 μm band is a proxy for hot dust content and their dust traces their gas. However, we see no mean offset in 12 μm luminosity between the galaxies detected and not detected in CO.

Both samples were selected to have a variety of times elapsed since the starburst (post-burst age). If the molecular gas is depleted over time, younger post-starbursts may be easier to detect in CO. While there is a shift toward detections with younger post-starburst ages, it is not statistically significant. The relation between molecular gas content and age since the burst is not straightforward, and is heavily dependent on the pre-burst gas mass of the galaxy and on the mechanics of the burst itself.

Because no statistically significant boost in CO detections occurs with either younger post-burst age or higher 12 μm luminosity, the molecular gas properties of our sample here are not significantly biased by the selection criteria. Therefore, our sample is likely to have a molecular gas detection rate representative of the overall post-starburst population.

4.2. Effect of Spatial Distributions of Gas and Stars

In Section 3.3, we made the assumptions that both the CO and current star formation were well-traced by the optical light, in order to calculate their surface densities. This is a good assumption for star-forming galaxies (Regan et al. 2001; Leroy et al. 2008; Schruba et al. 2011), but may not apply to our sample, especially if the reason for the end of the starburst is a disruption of the gas. Additionally, the spatial extent of any residual star formation is unknown and may not overlap with the optical light, which is dominated (~60%–90%) by the A stars formed in the recent burst. Without resolved observations, we are limited in how accurately we can know the distributions of gas and current star formation. If the CO emission or any currently star forming regions have sizes different than the optical size, it might be possible to resolve the observed offset from the KS relation. First, we test these assumptions for the post-starburst sample by estimating the CO emitting size with a model for the CO emission. We continue here to assume that CO traces H_2 well, with a conversion factor of $\alpha_{CO} = 4$. Second, we use our estimate of the CO emitting size to compare the scaled amount of CO near the center of the galaxy to the SDSS fiber-based SFRs.

By comparing the CO emission in two differently sized beams, we can roughly constrain the CO emitting size by assuming a Gaussian model for the shape of the emitting region. We estimate the source size for each galaxy by combining the CO(2–1) line measurements from IRAM 30 m and SMT 10 m, using the method from Lavezzi et al. (1999). I_{CO}, the integrated line intensity, is related to the surface brightness, so it should scale with the convolved size of the beam and the source as

$$\frac{I_{SMT}}{I_{IRAM}} = \frac{\theta_s^2 + \theta_{b,IRAM}^2}{\theta_s^2 + \theta_{b,SMT}^2} \quad (6)$$

for the same line, assuming a Gaussian distribution of the CO emission, where θ_b are the different beam sizes for IRAM 30 m and SMT, $\theta_{b,SMT} = 1.2\lambda/D \approx 33$ arcsec, and $\theta_{b,IRAM} = 1.166\lambda/D \approx 11$ arcsec, with the different coefficients due to the taper of each telescope. The source size θ_s is then given by

$$\theta_s = \sqrt{\frac{I_{IRAM}\,\theta_{b,IRAM}^2 - I_{SMT}\,\theta_{b,SMT}^2}{I_{SMT} - I_{IRAM}}} \quad (7)$$

for a Gaussian source.

We estimate source sizes for the six galaxies with IRAM 30 m CO(1–0), CO(2–1) and SMT CO(2–1) detections. Because the measurement errors propagate nonlinearly, we use a Monte Carlo technique to estimate the formal error on the size estimates, excluding any systematic error from the Gaussian model assumption. Sizes are listed in Table 3, and plotted over SDSS postage stamp images in Figure 10.

Previous studies of star-forming galaxies have found comparable exponential scale lengths of the CO emission and optical

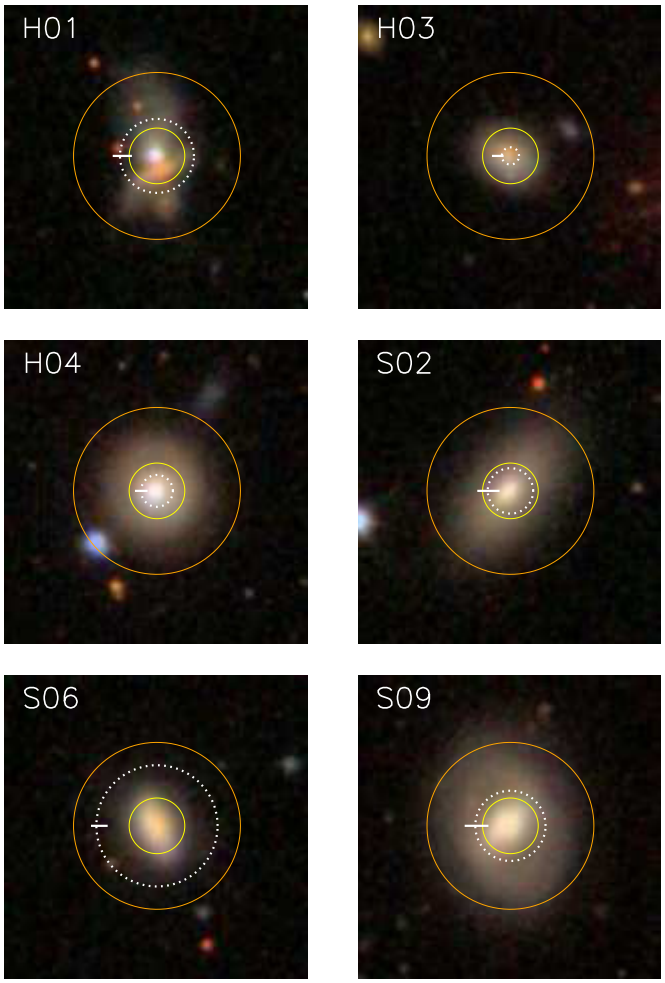

Figure 10. Estimated Gaussian half-light sizes of CO emitting regions (white dotted circles), with horizontal lines representing the Monte Carlo estimated error. FWHM beam sizes are shown for comparison: the inner yellow circle represents the IRAM 30 m CO(2–1) $\approx 11''$ beamsize, and the outer orange circle is the SMT CO(2–1) $\approx 33''$ beamsize. Optical images are from SDSS, and are $60'' \times 60''$. These CO sizes are $\sim 2\times$ the optical half-light sizes (not shown), due to the concentrated optical profile from the stars produced during the burst.

emission using resolved data (Regan et al. 2001; Leroy et al. 2008; Schruba et al. 2011). However, the CO to optical sizes are on average $\sim 2\times$ larger for our post-starburst sample, using either the optical half-light radii from an exponential fit or the Petrosian half-light radii. Because of the centrally peaked distribution of A stars in the post-starburst sample, this difference is due to the concentrated optical light, rather than extended CO emission. Concentrations measured for post-starburst galaxies (Yang et al. 2008) are high, consistent with the half light radii being smaller than for galaxies with an exponential profile.

To test the effect of assuming a Gaussian model, we perform a similar calculation for each galaxy, but for a uniform disk emitting region instead of a Gaussian. The half-light sizes for each source model are consistent within the measurement errors except for EAS06, where the uniform disk model predicts a size smaller than the Gaussian prediction ($20''$ versus $25''$).

The systematic errors associated with this method may be significant, especially as several of the estimated sizes are larger than the CO(2–1) IRAM 30 m beamsize. Thus, we use these sizes only to roughly estimate aperture bias in the CO observations, and to test whether use of this alternate size measure can eliminate the offset in the observed KS relation. The CO size estimates play no role in our main conclusions.

We use the CO emitting size estimates to model the effect of aperture bias in our CO(1–0) observations taken with the IRAM 30 m $\approx 22''$ beam. Given that the CO-emitting region is not a point source, the CO line luminosity calculated in Section 3.1 is likely an underestimate by a factor of $(\theta_s^2 + \theta_b^2)/\theta_b^2$, where θ_s and θ_b are the source and beam sizes, respectively. If we assume the mean CO source size of 9.2 kpc from our estimates above, then the corrections needed for the CO line luminosity, thus also $M(\mathrm{H_2})$ are ~ 1.1–$2.2\times$. The mean correction is an increase of $1.4\times$ from the original calculation, indicating that the molecular gas masses reported here may be conservative, with even higher amounts of molecular gas present.

Using the models of the CO emitting region that we construct from the size estimates and Gaussian assumption, we test the possibility that some of the observed CO does not participate in star formation. In Section 3.3, and in Figure 9, we assumed that all of the observed CO lay within the optical size R_{90}, which is always smaller than the IRAM 30 m CO(1–0) beamsize. Our CO size estimates, however, indicate that CO may extend beyond this aperture. We now estimate $\Sigma_{\mathrm{H_2}}$ within R_{90} by rescaling $M(\mathrm{H_2})$ using the Gaussian model to include only the gas mass within R_{90} (Figure 11 (left)). While still assuming that the current star formation is distributed like the optical light, this method allows us to compare the surface densities within the same aperture. In Section 3.1, we assumed that the source sizes were much smaller than the beam sizes to calculate $L'_{\mathrm{CO(1-0)}}$, but we now calculate Ω_{s*b} explicitly in Equation (1). Despite the decrease in $M(\mathrm{H_2})$ (and $\Sigma_{\mathrm{H_2}}$), the post-starburst sample is still significantly ($>4\sigma$) offset from the K98 galaxies. Allowing for the optical light and CO to be distributed differently does not change our results.

Next, we study the effect of allowing the spatial extent of any current star formation to differ from both the CO and optical light distributions. Swinbank et al. (2012) use resolved integral field unit observations of post-starburst galaxies, and find the nebular emission lines [O II] and [O III] to be spatially offset from the A star population in some cases, although these lines are particularly contaminated by LINER emission. If the current star formation is even more concentrated than the optical light, this could drive the observed offset of the post-starbursts on the KS relation. If this is the case, our assumptions about the aperture correction in the SFRs in Section 2.5 are not valid, and the SFRs are even more of an overestimate. We consider now the case where the star formation is restricted to the optical fiber.

Using the CO sizes estimates and Gaussian model, we rescale $M(\mathrm{H_2})$ to that within the $3''$ SDSS optical fiber, again with a Monte Carlo method to estimate the errors. We then estimate $\Sigma_{\mathrm{H_2}}$ inside the fiber aperture by scaling the CO luminosity, assuming a Gaussian profile with the CO size estimate. To calculate Σ_{SFR}, we use only the Hα flux from the fiber, not the aperture-corrected flux used elsewhere throughout this paper. We plot the resulting surface densities within the fiber apertures in Figure 11 (right). The post-starburst galaxies are still significantly offset from the K98 comparison galaxies. Thus, even if we allow for the possibility that some of the CO in the outer regions of the galaxy does not participate in star formation, or that the current star formation is more compact than the optical light, the offset from the K98 galaxies remains.

Even if the CO in the post-starburst sample and the K98 sample is distributed in the same way with respect to the optical light, aperture bias in the data sets could generate an apparent

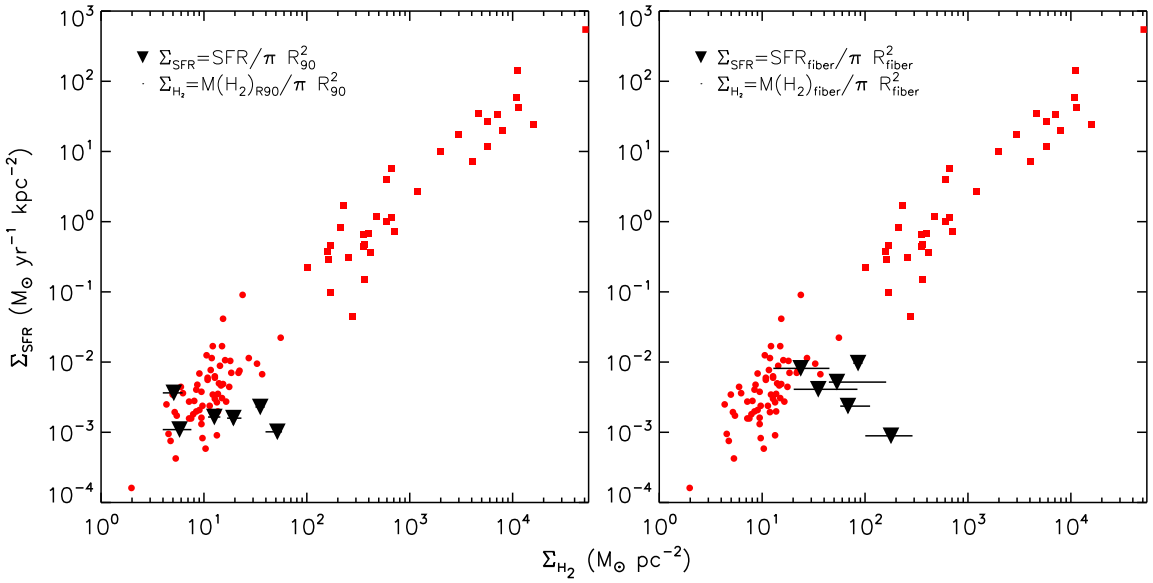

Figure 11. Alternative KS plots (red comparison points same as in Figure 9), accounting for possible spatial differences between molecular gas, star formation, and optical light. Left: Σ_{SFR} (from Hα) and Σ_{H_2} are both calculated within the optical radius R_{90} for the post-starburst sample. We use the CO size estimate from Section 4.2 and assume a Gaussian distribution to rescale $M(H_2)$ to that within R_{90} instead of within the larger IRAM 30 m 22″ beam as in Figure 9. Despite this rescaling, which allows for the possibility that the optical light and CO are distributed differently, we still observe an offset of the post-starburst galaxies from the K98 sample. Right: Σ_{SFR} and Σ_{H_2} are both calculated within the 3″ SDSS fiber. We rescale $M(H_2)$ to within this radius. SFR is calculated using only the Hα flux from the fiber, without rescaling. This is a test of whether the star formation is distributed differently than either the optical light or CO, and the continued offset shows that this possibility is unlikely unless the Gaussian assumption for the CO distribution is poor, or the star formation is even more concentrated within the fiber size.

offset. We do not see evidence of severe aperture bias in the post-starburst sample. Although we do observe higher molecular gas masses at higher redshifts, this is due to a combination of our decreased sensitivity and the higher stellar mass SDSS-selection at higher redshifts. We see no statistically significant trends with redshift of f_{gas}, or in the offset from the $n = 1.4$ power law KS relation from K98. If aperture bias only affected the post-starburst sample, it would result in an underestimation of the offset.

An offset could be generated, however, if the K98 sample was not measured out to the same physical radii as in the post-starburst sample. The CO isophotal sizes in the K98 star-forming sample are at most 60% of the optical isophotal sizes, and often much smaller. Galaxies with CO measured out to at least half the isophotal radii are the only ones included in the K98 sample. Assuming a worst-case, uniform disk distribution, the actual CO flux could be up to 70% higher than measured, which is not enough to resolve the observed offset of ∼400%.

The offset observed in Figure 8, that the post-starburst sample lies at lower SFR for a given $M(H_2)$ than other galaxies, and the similar robust offset in the KS relation (Figures 9 and 11), suggest that (1) the CO does not trace the H_2 as in our comparison galaxies or (2) the H_2 is not turning into stars in the same manner as our comparison galaxies (i.e., the SFE is lower or the IMF is bottom-heavy). We explore (1) in Section 4.3 and (2) in Section 4.4. For now we note that suppressing the SFE by allowing CO to extend beyond any current star formation region does not resolve the KS offset. Ultimately, interferometric CO observations will be required to test the spatial distribution of CO.

4.3. Effect of α_{CO} Choice

As discussed in Section 3, the CO to H_2 conversion factor (α_{CO}) is a known source of uncertainty in measuring molecular gas masses from CO observations. Here, we assume that H_2 traces the current star formation as expected for other galaxies, and explore variations in how CO traces the H_2.

So far, in plotting the KS relation we have assumed a single value of $\alpha_{CO} = 4$ for all samples. Now assuming a bimodal α_{CO} model instead, we apply a ULIRG-like value of $\alpha_{CO} = 0.8$ to the K98 starbursts and to our post-starburst sample, and leave the K98 star-forming galaxies with $\alpha_{CO} = 4$. We obtain the results in Figure 12 (top). This low value of α_{CO} applied to the post-starburst sample can remove their observed offset from the modified KS relation.

We can understand why starbursting galaxies may require a lower value of α_{CO} using the following toy model. α_{CO} is proportional to the column density of molecular gas $N(H_2)$ over the CO line intensity, as

$$\alpha_{CO} \propto \frac{N(H_2)}{I_{CO}} \propto \frac{N(H_2)}{T \times \sigma} \quad (8)$$

(Narayanan et al. 2011). In a merger, the column density is increased. However, the line intensity goes as the temperature T times the velocity dispersion σ, which both increase during the merger. In total, these factors result in a lower value of α_{CO}. After the merger, the gas kinetic temperature may decline to match conditions in early-type galaxies, but it is not clear what this simple model predicts for the post-starburst sample.

We cannot assume the post-starbursts will have a similar value of α_{CO} as ULIRGs or starbursts simply because they are the likely progenitors. We expect the physical state of the gas to have changed significantly in the 0.3–1 Gyr since the burst, as the dynamical timescales for ULIRGs are of order 10^6–$10^{7.5}$ yr (Genzel et al. 2010). However, if the state of the gas after the merger changes in such a way as to keep the gas heated, but as to lower the column density of molecular gas, α_{CO} may have a low value. Additionally, if an AGN heated the bulk of the molecular gas, the CO brightness temperature could increase for a given H_2 mass, lowering α_{CO}.

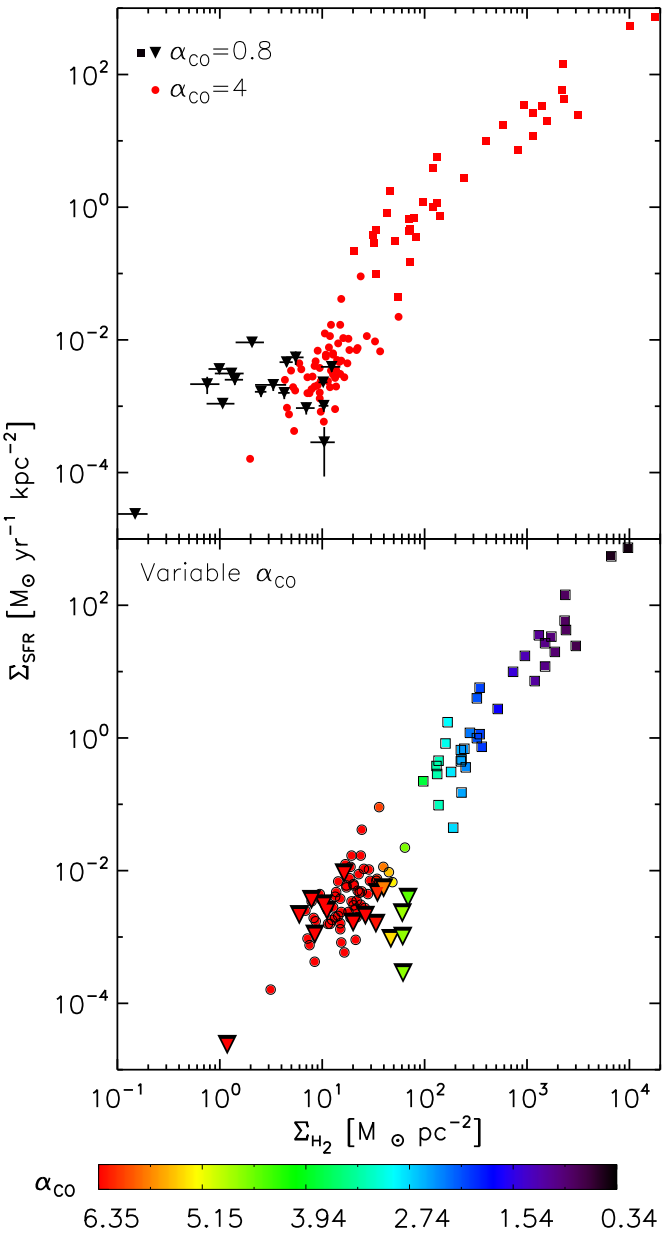

Figure 12. Top: same as Figure 9(a) (see description in Section 3.3), but assuming $\alpha_{CO} = 4$ for the K98 star-forming galaxies, and $\alpha_{CO} = 0.8$ for the K98 starbursts and our post-starburst sample. Here, the offset previously observed can be reconciled by assuming a ULIRG-type value of $\alpha_{CO} = 0.8$ for the post-starburst sample. Bottom: same as Figure 9, but now assuming the variable α_{CO} for the K98 sample and post-starburst sample using the formula from Narayanan et al. (2012). As before, triangles, circles, and squares represent the post-starburst sample, K98 star-forming galaxies, and K98 starbursts, respectively. We still observe a systematic shift low on the Kennicutt–Schmidt relation, which suggests that the variable α_{CO} model does not resolve the differences between the post-starbursts and other galaxies.

If much of the CO emission comes from outside of GMCs, the CO(1–0) linewidth could be strongly affected by the gravitational potential in the galaxy, instead of just by its own turbulence (Downes & Solomon 1998). The fact that starbursts have more diffuse gas, and less gas bound in molecular clouds, has been used as justification for their low values of α_{CO}. We can estimate the influence of the stellar potential on α_{CO} using the prescription from Bolatto et al. (2013). They suggest that α_{CO} scales down from the Galactic value as $\alpha_{CO}/\alpha_{CO,MW} = (\Sigma_{total}/100\ M_\odot\,pc^{-2})^{-0.5}$, where Σ_{total} is the combined surface density of stars and gas. Adding the stellar mass to the molecular gas mass, and calculating the surface density within the optical radius R_{90}, our post-starbursts have total surface densities of 130–460 $M_\odot$ pc^{-2}, predicting $\alpha_{CO} = 1.9$–3.5, scaled down from the Galactic value of $\alpha_{CO} = 4$. This difference between the assumed α_{CO} for comparison star-forming galaxies and the post-starburst sample is not enough to resolve their observed offset. However, this relation is subject to scatter, and there may be significant variation in the influence of diffuse gas on α_{CO} (Liszt & Pety 2012).

The use of a bimodal α_{CO} is not necessarily physical (although see, e.g., Tacconi et al. 2008; Daddi et al. 2009), because a variety of ISM conditions should exist, resulting in a continuum of α_{CO} values. In particular, because post-starburst galaxies may be at an intermediate stage between being dynamically hot and more relaxed, the appropriate α_{CO} for these systems may lie between the Galactic average and the typical value used for ULIRGs. The Narayanan et al. (2012) formulation suggests that α_{CO} varies smoothly with galaxy physical properties, and may be parametrized in terms of the gas phase metallicity and the CO surface brightness. Our galaxies do not have abnormal metallicities. Goto (2007) study the metallicities of post-starburst galaxies and do not find them to be anomalous. The mass–metallicity relation (Tremonti et al. 2004) also predicts metallicities that are similar to the comparison galaxies, so we vary α_{CO} only with CO brightness. The result of applying this variable α_{CO} model to both the post-starburst and K98 samples can be seen in Figure 12 (bottom). The variable α_{CO} model does not remove the offset.

We are unable to rule out a low value of $\alpha_{CO} = 0.8$ as a potential explanation for the offset from the KS relation. We can resolve this question observationally using higher J_{up} lines of CO to constrain the temperature and density of the gas, as well as with denser gas tracers such as HCN to probe denser regions of the gas, bypassing the uncertainties arising from any CO outside of GMCs.

4.4. Implications for Galaxy Evolution

Our findings that post-starburst galaxies can have large gas reservoirs, and that they are offset low from the KS relation, help to discriminate among the physical processes proposed to end the burst. Clearly, scenarios that require the molecular gas to be absent, such as the complete (1) expulsion or removal of the gas (e.g., in outflows or some environmental mechanisms; Feruglio et al. 2010; Rupke & Veilleux 2011; Boselli & Gavazzi 2006), (2) consumption of the gas in the burst, and (3) prevention of gas infall into the galaxy and of the subsequent formation of new GMCs ("starvation"; Larson et al. 1980), are now excluded, at least in the half of our sample with detected molecular gas. Alternatively, the molecular gas within the galaxies could be (4) heated (Nesvadba et al. 2010), (5) kinematically prevented from collapsing into GMCs ("morphological quenching"; Martig et al. 2009), or (6) dispersed. Here, we comment on the implications of our results for these latter scenarios, and on what data are needed to complete the picture.

The offset observed in both Figures 8 and 9 could be caused by either a breakdown in the relation between CO and H_2 (a different value of α_{CO}), or between H_2 and the SFR (a different SFE), such that either is different than for the comparison galaxies. The burst-ending mechanisms of molecular gas heating (scenario 4) or morphological quenching (scenario 5) might alter the state of the gas relative to normal star-forming galaxies, acting to lower α_{CO} (see Equation (5))

or to reduce the SFE for a given $M(H_2)$. In the case where α_{CO} *is* low, dispersal of the gas (scenario 6) would drive the post-starbursts down along the KS relation.

Analyzing the gas state is outside the scope of this paper, as we cannot constrain the temperature or density of the CO emitting region using only the CO(1–0) and (2–1) lines (e.g., Carilli & Walter 2013). We need higher J_{up} lines and denser gas tracers to do so. Determining if the galaxy is undergoing morphological quenching requires resolved kinematics of the molecular gas. If the offset from the KS relation is not due to incorrect assumptions about α_{CO} (see Section 4.3), the SFR (Section 2.5), or the relative spatial distribution of H_2, optical light, and star formation (Section 4.2, assuming CO traces H_2), the intriguing possibility of a lower SFE in post-starbursts remains.

Another potential explanation for the offset is that our galaxies are still forming stars, but with a bottom-heavy IMF dominated by low mass stars that are not detectable by our SFR indicators. Regardless of the IMF during the burst, any subsequent star formation in our sample might be expected to track that of early types, for which bottom-heavy IMFs have been suggested (e.g., van Dokkum & Conroy 2010). We test this hypothesis by estimating the change in the Hα-derived SFRs with IMF slope. For consistency, so far we have used the same conversion factor from $L(H\alpha)$ to SFR as K98, who employed a Salpeter IMF ($x = 2.35$ slope). However, van Dokkum & Conroy (2010) favor a steeper, more bottom-heavy slope of $x = 3$. We use Starburst 99 v7.0.0 (Leitherer et al. 2014) models with a variety of IMF slopes over the range 0.1–1 $M_\odot$. For a bottom-heavy IMF slope of $x = 3$, we would underestimate the SFR significantly (by $\sim$20×), more than enough to explain the offset of our galaxies from the KS relation.

5. CONCLUSIONS

We study molecular gas in a sample of 32 nearby ($0.01 < z < 0.12$) post-starburst (aka "E+A") galaxies, whose optical spectra indicate a recent starburst that ended within the last $\sim$Gyr. We target the CO lines (1–0) and (2–1) with the IRAM 30 m and SMT 10 m telescopes, constraining the molecular gas mass remaining in these galaxies after the starburst. Our conclusions are as follows:

1. Molecular gas is detected in 17 (53%) galaxies with CO(1–0) observations from the IRAM 30 m. We obtain molecular gas masses of $M(H_2) = 10^{8.6}$–$10^{9.8}\,M_\odot$ $(\alpha_{CO}/4\,M_\odot\ (K\,km\,s^{-1}\,pc^2)^{-1})$, and molecular gas to stellar mass fractions of $f_{gas} \sim 10^{-2}$–$10^{-0.5}$ $(\alpha_{CO}/4\,M_\odot\ (K\,km\,s^{-1}\,pc^2)^{-1})$, roughly comparable to those of star-forming galaxies and generally larger than for early types, for a range of likely CO-to-H_2 conversion factors (α_{CO}). The upper limits on $M(H_2)$ for the 15 undetected galaxies range from $10^{7.7}\,M_\odot$ to $10^{9.7}\,M_\odot$, with the median more consistent with early-type galaxies than with star-forming galaxies.
2. We compare $M(H_2)$ to the SFR, using Hα and $D_n(4000)$ to calculate upper limits on the current SFR in this sample. When compared to other star-forming, starbursting, and early type galaxies, the post-starbursts have $\sim$10–20× lower SFRs for a given $M(H_2)$.
3. The post-starburst sample falls $\sim$4× below other local galaxies on the KS relation (Kennicutt 1998) of SFR surface density versus $M(H_2)$ surface density. The median locus of the post-starburst galaxies is offset from the relation defined by normal star-forming galaxies (K98) at 5σ significance. After considering sample selection effects, aperture bias, varying spatial extents of current star formation, optical light and H_2, CO not tracing H_2 (a different α_{CO}), and the effect of IMF assumptions, we conclude the observed offset is likely due to suppressed SFE, a low value of α_{CO} consistent with ULIRGs, and/or a bottom-heavy IMF.

Our results show that the end of the starburst in these galaxies cannot be attributed to the complete consumption, expulsion, or starvation of the molecular gas reservoirs. Resolved interferometric CO maps of these galaxies, higher J_{up} lines of CO for density–temperature constraints, denser gas tracers such as HCN, and resolved star formation maps are necessary to more thoroughly study the current state of gas in post-starbursts, and to more accurately compare to the residual star formation. Understanding this possibly common phase in galaxy evolution will help reveal the physics of star formation in galaxies as well as their evolution through mergers.

We thank Adam Smercina for helpful discussions regarding his ongoing analysis of the dust emission from the post-starburst sample. Based on observations carried out with the IRAM-30 m Telescope and the ARO SMT 12 m. IRAM is supported by INSU/CNRS (France), MPG (Germany) and IGN (Spain). The SMT is operated by the Arizona Radio Observatory (ARO), Steward Observatory, University of Arizona. We thank Dennis Zaritsky for his suggestion to explore a bottom-heavy IMF. We thank the operators and staff of the ARO. K.D.F. is supported by NSF grant DGE-1143953. A.I.Z. thanks the John Guggenheim Foundation and the Center for Cosmology and Particle Physics at NYU. A.I.Z. acknowledges support from NASA ADP grant 3227400 and NSF grant 3002520. D.N. acknowledges financial support from the NSF via awards AST-1009452 and AST-1442650. Funding for the Sloan Digital Sky Survey (SDSS) has been provided by the Alfred P. Sloan Foundation, the Participating Institutions, the National Aeronautics and Space Administration, the National Science Foundation, the U.S. Department of Energy, the Japanese Monbukagakusho, and the Max Planck Society. The SDSS Web site is http://www.sdss.org/.

Facilities: IRAM:30m, HTT

Note added in proof. A recent preprint on the evolution of cold molecular gas from the starburst to early post-starburst stage was posted late in our refereeing process. Rowlands et al. (2015) find molecular gas reservoirs similar to those found here. However, the two samples do not overlap as their selection methods are very different. Their post-starburst sample includes some galaxies that are still in the late stages of their starburst, with SFRs from < 0.2 to $9\,M_\odot\,yr^{-1}$, higher than for our sample, which spans 10^{-2} to $1\,M_\odot\,yr^{-1}$ and likely leads to the significant offset that we observe from the Kennicutt–Schmidt relation.

REFERENCES

Abazajian, K. N., Adelman-McCarthy, J. K., Agüeros, M. A., et al. 2009, ApJS, 182, 543
Aihara, H., Allende Prieto, C., An, D., et al. 2011, ApJS, 193, 29
Alatalo, K., Nyland, K., Graves, G., et al. 2014, ApJ, 780, 186
Baldwin, J. A., Phillips, M. M., & Terlevich, R. 1981, PASP, 93, 5
Becker, R. H., White, R. L., & Helfand, D. J. 1995, ApJ, 450, 559
Bolatto, A. D., Wolfire, M., & Leroy, A. K. 2013, ARA&A, 51, 35
Boselli, A., & Gavazzi, G. 2006, PASP, 118, 517
Bressan, A., Silva, L., & Granato, G. L. 2002, A&A, 392, 377
Brinchmann, J., Charlot, S., White, S. D. M., et al. 2004, MNRAS, 351, 1151
Bruzual, G., & Charlot, S. 2003, MNRAS, 344, 1000

Buyle, P., Michielsen, D., De Rijcke, S., et al. 2006, ApJ, 649, 163
Cappellari, M., Emsellem, E., Krajnović, D., et al. 2011, MNRAS, 413, 813
Carilli, C. C., & Walter, F. 2013, ARA&A, 51, 105
Casey, C. M., Narayanan, D., & Cooray, A. 2014, PhR, 541, 45
Chang, T.-C., van Gorkom, J. H., Zabludoff, A. I., Zaritsky, D., & Mihos, J. C. 2001, AJ, 121, 1965
Chen, Y.-M., Kauffmann, G., Tremonti, C. A., et al. 2012, MNRAS, 421, 314
Choi, P. I., Yan, L., Im, M., et al. 2006, ApJ, 637, 227
Condon, J. J. 1992, ARA&A, 30, 575
Condon, J. J., Cotton, W. D., Greisen, E. W., et al. 1998, AJ, 115, 1693
Couch, W. J., & Sharples, R. M. 1987, MNRAS, 229, 423
Crocker, A. F., Bureau, M., Young, L. M., & Combes, F. 2011, MNRAS, 410, 1197
Daddi, E., Dannerbauer, H., Krips, M., et al. 2009, ApJ, 695, L176
Davis, T. A., Young, L. M., Crocker, A. F., et al. 2014, MNRAS, 444, 3427
de Vries, W. H., Hodge, J. A., Becker, R. H., White, R. L., & Helfand, D. J. 2007, AJ, 134, 457
Downes, D., & Solomon, P. M. 1998, ApJ, 507, 615
Dressler, A., & Gunn, J. E. 1983, ApJ, 270, 7
Feruglio, C., Maiolino, R., Piconcelli, E., et al. 2010, A&A, 518, 4
Gao, Y., & Solomon, P. M. 2004, ApJ, 606, 271
Genzel, R., Tacconi, L. J., Gracia-Carpio, J., et al. 2010, MNRAS, 407, 2091
Goto, T. 2007, MNRAS, 377, 1222
Hayward, C. C., Lanz, L., Ashby, M. L. N., et al. 2014, MNRAS, 445, 1598
Kauffmann, G., Heckman, T. M., White, S. D. M., et al. 2003a, MNRAS, 341, 33
Kauffmann, G., Heckman, T. M., Tremonti, C., et al. 2003b, MNRAS, 346, 1055
Kennicutt, J. 1998, ApJ, 498, 541
Kennicutt, R. C., Hao, C.-N., Calzetti, D., et al. 2009, ApJ, 703, 1672
Kennicutt, R. C., Tamblyn, P., & Congdon, C. E. 1994, ApJ, 435, 22
Kennicutt, R. C., Jr., Calzetti, D., Walter, F., et al. 2007, ApJ, 671, 333
Kewley, L. J., Dopita, M. A., Sutherland, R. S., Heisler, C. A., & Trevena, J. 2001, ApJ, 556, 121
Kohno, K., Tosaki, T., Matsushita, S., et al. 2002, PASJ, 54, 541
Larson, R. B., Tinsley, B. M., & Caldwell, C. N. 1980, ApJ, 237, 692
Lavezzi, T. E., Dickey, J. M., Casoli, F., & Kazès, I. 1999, AJ, 117, 1995
Leitherer, C., Ekström, S., Meynet, G., et al. 2014, ApJS, 212, 14
Leroy, A. K., Walter, F., Brinks, E., et al. 2008, AJ, 136, 2782
Liszt, H. S., & Pety, J. 2012, A&A, 541, A58
Maraston, C., & Strömbäck, G. 2011, MNRAS, 418, 2785
Martig, M., Bournaud, F., Teyssier, R., & Dekel, A. 2009, ApJ, 707, 250
Morić, I., Smolčić, V., Kimball, A., et al. 2010, ApJ, 724, 779
Narayanan, D., Cox, T. J., Kelly, B., et al. 2008, ApJS, 176, 331
Narayanan, D., Krumholz, M., Ostriker, E. C., & Hernquist, L. 2011, MNRAS, 418, 664
Narayanan, D., Krumholz, M. R., Ostriker, E. C., & Hernquist, L. 2012, MNRAS, 421, 3127
Nesvadba, N. P. H., Boulanger, F., Salomé, P., et al. 2010, A&A, 521, A65
Norton, S. A., Gebhardt, K., Zabludoff, A. I., & Zaritsky, D. 2001, ApJ, 557, 150
O'Donnell, J. E. 1994, ApJ, 422, 158
Petrosian, V. 1976, ApJL, 209, L1
Regan, M. W., Thornley, M. D., Helfer, T. T., et al. 2001, ApJ, 561, 218
Rich, J. A., Kewley, L. J., & Dopita, M. A. 2011, ApJ, 734, 87
Rowlands, et al. 2015, MNRAS, in press (arXiv:1412.6090)
Rupke, D. S. N., & Veilleux, S. 2011, ApJL, 729, L27
Saintonge, A., Kauffmann, G., Kramer, C., et al. 2011, MNRAS, 415, 32
Saintonge, A., Tacconi, L. J., Fabello, S., et al. 2012, ApJ, 758, 73
Salim, S., Rich, R. M., Charlot, S., et al. 2007, ApJS, 173, 267
Schawinski, K., Lintott, C. J., Thomas, D., et al. 2009, ApJ, 690, 1672
Schruba, A., Leroy, A. K., Walter, F., et al. 2011, AJ, 142, 37
Sell, P. H., Tremonti, C. A., Hickox, R. C., et al. 2014, MNRAS, 441, 3417
Singh, R., van de Ven, G., Jahnke, K., et al. 2013, A&A, 558, A43
Snyder, G. F., Cox, T. J., Hayward, C. C., Hernquist, L., & Jonsson, P. 2011, ApJ, 741, 77
Solomon, P. M., Downes, D., Radford, S. J. E., & Barrett, J. W. 1997, ApJ, 478, 144
Strauss, M. A., Weinberg, D. H., Lupton, R. H., et al. 2002, AJ, 124, 1810
Swinbank, A. M., Balogh, M. L., Bower, R. G., et al. 2012, MNRAS, 420, 672
Tacconi, L. J., Genzel, R., Smail, I., et al. 2008, ApJ, 680, 246
Tremonti, C. A., Heckman, T. M., Kauffmann, G., et al. 2004, ApJ, 613, 898
Tremonti, C. A., Moustakas, J., & Diamond-Stanic, A. M. 2007, ApJL, 663, L77
Utomo, D., Kriek, M., Labbé, I., Conroy, C., & Fumagalli, M. 2014, ApJL, 783, L30
van Dokkum, P. G., & Conroy, C. 2010, Natur, 468, 940
Wong, O. I., Schawinski, K., Kaviraj, S., et al. 2012, MNRAS, 420, 1684
Yamauchi, C., & Goto, T. 2005, MNRAS, 359, 1557
Yan, R., Newman, J. A., Faber, S. M., et al. 2006, ApJ, 648, 281
Yang, Y., Tremonti, C. A., Zabludoff, A. I., & Zaritsky, D. 2006, ApJL, 646, L33
Yang, Y., Zabludoff, A. I., Zaritsky, D., Lauer, T. R., & Mihos, J. C. 2004, ApJ, 607, 258
Yang, Y., Zabludoff, A. I., Zaritsky, D., & Mihos, J. C. 2008, ApJ, 688, 945
York, D. G., Adelman, J., Anderson, J. E., Jr., et al. 2000, AJ, 120, 1579
Young, L. M., Bureau, M., Davis, T. A., et al. 2011, MNRAS, 414, 940
Zabludoff, A. I., Zaritsky, D., Lin, H., et al. 1996, ApJ, 466, 104
Zwaan, M. A., Kuntschner, H., Pracy, M. B., & Couch, W. J. 2013, MNRAS, 432, 8